MODIFICATION OF GLASSY CARBON UNDER STRONTIUM ION IMPLANTATION

by

OPEYEMI SHAKIRAH ODUTEMOWO

Submitted in partial fulfilment of the requirements for the degree of

MAGISTER SCIENTIAE

In the Faculty of Natural and Agricultural Sciences at University of Pretoria

October..2013

Supervisor/Promoter: Prof J.B. Malherbe

SUMMARY

Modification of glassy carbon under strontium ion implantation

By

Opeyemi Shakirah Odutemowo

Submitted in partial fulfilment of the requirements for the degree of (Msc) in Physics in the Faculty of Natural and Agricultural Science, University of Pretoria

Supervisor/Promoter: Prof. J.B. Malherbe

Glassy carbon is a disordered form of carbon with very high temperature resistance, high hardness and strength and chemical stability even in extreme environments. Glassy carbon is also unaffected by nearly all acids and cannot be graphitized even at very high temperature. Because of these characteristics, there is a possibility that glassy carbon can replace copper, iron, titanium alloys and other materials employed in making canisters used in nuclear waste storage.

The modification of glassy carbon due to strontium ions implantation and heat treatment is reported. Glassy carbon (GC) samples were implanted with 200 keV strontium ions to a fluence of 2×10^{16} ions/cm^2 at room temperature.

Sequential isochronal annealing was carried out on the implanted samples at temperatures ranging from 200 ^{o}C - 900 ^{o}C for one hour. The influence of ion implantation and annealing on surface topography was examined by the scanning electron microscopy (SEM), while Raman spectroscopy was used to monitor the corresponding structural changes induced in the glassy carbon. The depth profiles of the implanted strontium before and after annealing were determined using Rutherford Backscattering Spectroscopy (RBS).

Compared to SRIM predictions the implanted strontium profiles was broader. After annealing at 300 ^{o}C, bulk and surface diffusion of the strontium atoms took place. Annealing at 400 ^{o}C- 700 ^{o}C not only resulted in further diffusion of strontium towards the surface, the diffusion was accompanied with segregation of strontium on the surface of the glassy carbon substrate. Evaporation of the strontium atoms was noticed when the sample was annealed at 800 ^{o}C and 900 ^{o}C respectively. These annealing temperatures are higher than the melting point of strontium (~769 ^{o}C).

The Raman spectrum of the virgin glassy carbon shows the disorder (D) and graphitic (G) peaks which characterize disordered carbon materials. Merging of these two peaks was observed when the virgin sample was implanted with strontium ions. Merging of these peaks is due to damage caused by the implantation of strontium. The Raman spectrum recorded after heat treatment showed that only some of the damage due to implantation was annealed out. Annealing at 2000^{0}C for 5 hours resulted in a Raman spectrum very similar to that of virgin glassy carbon indicating that the damage due to the ion implantation was annealed out.

SEM showed large differences in the surface topography of the polished glassy carbon surfaces and those of as-implanted samples. Annealing did not significantly change the surface microstructure of the implanted samples.

UNIVERSITEIT VAN PRETORIA
UNIVERSITY OF PRETORIA
YUNIBESITHI YA PRETORIA

DECLARATION

I, Opeyemi Shakirah Odutemowo, declare that the dissertation, which I hereby submit for the degree of MSc in University of Pretoria, is my own work and has not been submitted by for a degree at this or any other tertiary institution.

Signature: …….

Date: …….

UNIVERSITEIT VAN PRETORIA
UNIVERSITY OF PRETORIA
YUNIBESITHI YA PRETORIA

Acknowledgements

I will like to acknowledge the following people for their support and valuable contribution in the success of my study.

- My academic promoter, Prof. J.B. Malherbe, Mr D.F Langa, and Dr N. van de Berg for their guidance, support, discussion during the course of this study.

- The head of department, Prof. C.C Theron , for arranging some part-time work in the department, which helped me financially during this study.

- Mr J. Smith, Dr. T.T. Hlatswayo and Mr Eric Njoroge for all the help they provided with the accelerator.

- Dr L. Prinsloo for her assistance with Raman spectroscopy.

- Fellow students in the Physics department, Chemist Mabena, Thabsile Thabethe, Eric Njoroge, Cecil Ouma, Joseph Kuhudzai, Lesolle Sebtila and Kingsley Obodo for all their help, encouragement and moral support.

- My family for their endless love, support and encouragement throughout my studies and life.

- God for his general awesomeness.

TABLE OF CONTENTS.

CHAPTER 1

INTRODUCTION

The burning of fossil fuels to generate electricity has led to numerous environmental problems such as global warming, greenhouse effect and urban smog. Most countries including developing countries are now looking into having a cleaner alternative for power generation [Bro91].

Nuclear energy is a cleaner alternative way of generating electricity because of its environmental benefits. Nuclear plants do not emit gases such as nitrogen oxide, sulfur dioxide, carbon dioxide or other gases that could endanger the environment by causing greenhouse effect, acid rain, global warming etc.

The other advantages of using nuclear energy as an alternative source of electricity generation include the following; nuclear power plants do not require lots of space when compared to wind farms and solar fields. It also has a lower fuel and running cost compared to fossil fuels power plants. It has a more stable power when compared to renewable energy power sources. The volume of waste generated is very low when compared to the burning of fossil fuels.

Despite all the advantages of using nuclear energy in lieu of fossil fuels, it is still the most controversial source of power generation because of the toxicity of the wastes generated, the difficulties in the storage of the wastes produced and the dangers associated with nuclear reactors.

Because of the environmental and health hazards associated with nuclear waste i.e. fission products, there is a need to store them in containers made of suitable materials that can contain them for a long period of time before they are moved to a more permanent site.

1.1 CHARACTERIZATION OF NUCLEAR WASTES.

Nuclear fission of uranium produces by-products such as cesium, barium, silver, strontium, xenon, iodine and krypton. These wastes are characterized as low level waste, mill tailings waste or high level waste [Com96]. The differences between these levels and methods of storage for these wastes will be discussed in this section.

1.1.1 HIGH LEVEL NUCLEAR WASTES [HLW].

High level nuclear wastes (HLW) consist of spent nuclear fuels from commercial power plants and military facilities. These wastes are spent fuels derived from nuclear fuels that have been used in the reactor for a period of time. These spent nuclear fuels are highly toxic and radioactive. Some of these nuclear wastes have very short half-lives but most of them have very long half-lives. An example of a high level nuclear waste element with long half-life is plutonium-239 with half-life of 24000 years [Com96]. Exposure to high level nuclear wastes can result in health problems such as cancer, increase in environmental temperature and radiation. Strontium-90 is characterized as a high level nuclear waste element.

1.1.2 MILL TAILINGS WASTES.

Mill tailings wastes are residues remaining after the processing of natural ore to obtain uranium and thorium [Com96]. These tailings contain radioactive elements including uranium, thorium, radium, polonium and radon. Generally, the radiation contained in mill tailings is far less than high level nuclear wastes (HLW), however, some of the isotopes in these tailings have long half-lives and they can be hazardous for many years. Disposal of mill tailings is one of the most important environmental issues especially in developing nations as most of these nations do not take significant steps to mitigate environmental consequences [www3].

1.1.3 LOW LEVEL NUCLEAR WASTES [LLW].

Low level nuclear wastes include all other radioactive wastes excluding spent fuels, transuranic materials, mill tailings. They are mostly generated from industries like pharmaceutical plants, university laboratories and medical facilities.

1.2 STRONTIUM AS A NUCLEAR WASTE.

Strontium is an alkaline-earth metal with atomic number 38. It occurs mostly in combination with other elements because of its extreme reactivity with air. Strontium occurs mostly as sulfate mineral Celestite ($SrSO_4$) and strontium carbonate ($SrCO_3$). It has mostly the same applications as calcium and barium.

1.2.1 ISOTOPES OF STRONTIUM.

Strontium has four stable isotopes which are naturally occurring. The table below gives information about natural occurring isotopes of strontium.

Table 1: Atomic mass and natural abundance of the four stable isotopes of strontium.

ISOTOPE	ATOMIC MASS	NATURAL ABUNDANCE (%)
^{84}Sr	83.91	0.56
^{86}Sr	85.90	9.86
^{87}Sr	86.90	7.00
^{88}Sr	87.90	82.58

In addition to the four stable isotopes, strontium has about sixteen unstable isotopes. The most important of them all are ^{90}Sr and ^{89}Sr. ^{90}Sr comes from three major sources; fallout from above-ground explosions of nuclear weapons testing worldwide from 1963-1980, radioactive releases from the 1986 Chernobyl nuclear power accident in the Ukraine and radioactive releases from nuclear power plants into the environment [Com96].

Strontium-90 has been tipped to be the most dangerous component from nuclear fallout and accidents because of its ability to displace calcium from the bones. Despite this characteristic, strontium-90 has been used extensively in medicine, as radioactive tracers and also in space craft engineering. Stronitium-89 has been used extensively for treatment of bone cancer.

Strontium-89 and strontium-90 isotopes can be generated with these possible fission reactions:

$$^{236}_{92}\mathrm{U} \rightarrow {}^{90}_{38}\mathrm{Sr} + {}^{144}_{54}\mathrm{Xe} + 2\,{}^{0}\mathrm{n} + \text{energy} \qquad 1.1$$

$$^{235}_{92}\mathrm{U} \rightarrow {}^{89}_{38}\mathrm{Sr} + {}^{143}_{53}\mathrm{Xe} + 3{}^{0}\mathrm{n} + \text{energy} \qquad 1.2$$

The table below gives information about some unstable isotopes of strontium.

Table 2: Mass, half-life and mode of decay of some unstable isotopes of strontium [www2].

ISOTOPE	**MASS**	**HALF-LIFE**	**MODE OF DECAY**
^{80}sr	79.92453	1.77 hours	Electron capture [EC] to ^{80}Rb
^{81}Sr	80.92322	22.3minutes	EC to ^{81}Rb
^{82}Sr	81.91840	25.36 days	EC to ^{82}Rb
^{83}Sr	82.91756	1.350 days	EC to ^{83}Rb
^{85}Sr	84.912936	64.85days	EC to ^{85}Rb
^{89}Sr	88.907455	50.52 days	β^- to ^{89}Y
^{90}Sr	89.907738	29.1 years	β^- to ^{90}Y

1.2.2 STORAGE OF NUCLEAR WASTES.

Performance of materials used is storing nuclear wastes is very important when the issue of nuclear waste management is concerned as these determines the safety of these wastes. A waste container should be able to provide barriers against physical and chemical stress during transportation, interim storage and disposal of waste products. A waste container should be able to resist chemical attacks, thermal attacks and must be relatively inexpensive [Yim00].

Nuclear wastes are usually stored in canisters made of metals such as iron, nickel-based alloys, stainless steel etc. These materials have their shortcomings and disadvantages when used to store these wastes. Some of the materials and their shortcomings are listed below:

i. Copper is known to have very good environmental stability but it is however known to be poor in brine and in a radiation environment [Wer92].
ii. Stainless steel has good mechanical properties and is also corrosive resistant; however, it is prone to catastrophic failures.
iii. Titanium alloys are mechanically strong and have very good corrosion resistance but they can experience brittle failure.
iv. Nickel based alloys are also corrosive resistant but highly expensive [Yim00].

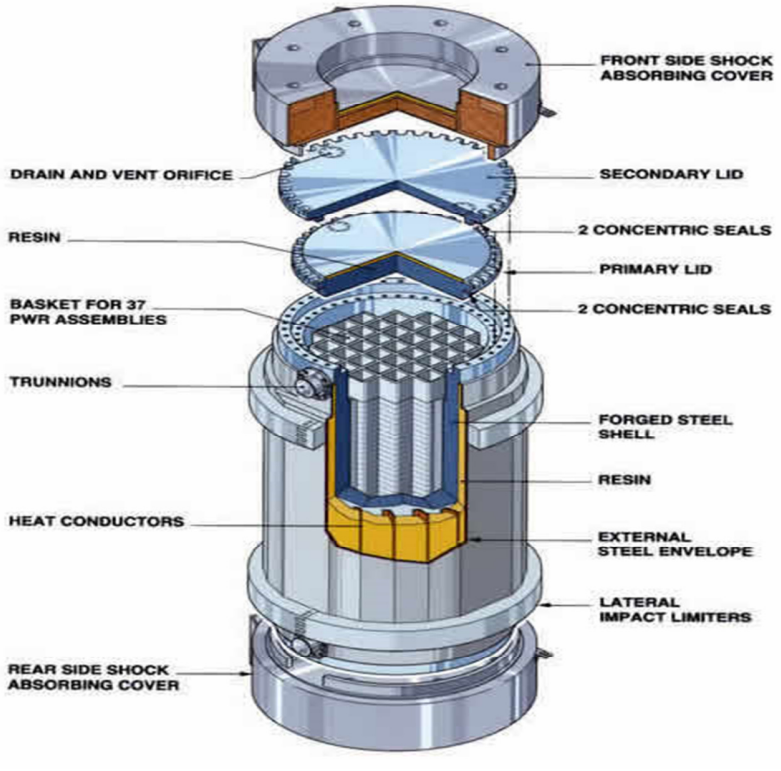

Figure 1: A typical configuration for a used fuel canister [www1].

1.3 GLASSY CARBON

Glassy carbon (also known as vitreous carbon) is an advanced material of carbon combining glass, ceramic and graphitic properties [Htw06]. It is frequently called polymeric carbon since it is derived mostly from the carbonization of polymeric precursor [Pie93].

In this research, Sigradur® G glassy carbon samples were used. The properties of glassy carbon that differentiates it from other carbon materials including graphite are its;

i. **High temperature resistance:** glassy carbon is a non-graphitizing carbon and cannot be transformed into crystalline graphite even at temperatures above 3000^{0}C.

ii. **Resistance to chemical attacks:** the rate of oxidation of glassy carbon in oxygen, carbon dioxide and water vapour has been found to be lower than that of other carbon material[Har04].

iii. **High resistant to attacks by acids:** glassy carbon is not affected when it comes in contact with concentrated sulphuric and nitric acids at room temperature even when it has been exposed for several months. Graphite on the other hand turns to powder when it comes into contact with these acids.

iv. **Extreme corrosion resistance:** the closed structure of glassy carbon does not permit it to form intercalation compounds. This feature makes it difficult for it to be corroded by acids and alkali agents.

v. **High hardness and strength:** unlike most graphitic and ceramic materials, glassy carbon increases with strength with a rise in temperature up to 2700 K.

The properties of glassy carbon also include; high purity, impermeability to gas and liquids, no wetting by melts, low density, low thermal expansion, good electrical conductivity and extreme resistance to thermal shock.

Table 3: Physical properties of SIGRADUR®G glassy carbon samples used in this research (as obtained from the manufacturer).

Maximum service temperature (vacuum and inert gas)	3000 ^{o}C
Density	1.42 g/cm^3
Open porosity	0%
Permeability coefficient	10^{-9} cm^2/s
Vickers hardness	230 HV
Flexural strength	260 MPa
Young's modulus	35 GPa
Compressive strength	480 MPa
Specific electrical resistance (30 ^{0}C)	45 Ωμm
Thermal conductivity (30 ^{0}C)	6.3 W/(km)
Median linear coefficient of expansion (20-200 ^{0}C)	2.6×10^{-6}/K

The table above gives the physical properties of the SIGRADUR® G glassy carbon used throughout this research. This information was obtained from the manufacturer's website.

1.3.1 STRUCTURE OF GLASSY CARBON

The glassy carbon is a form of carbon with highly disordered structure. The high strength, high Young's modulus, high hardness and high impermeability to gases of glassy carbon suggest that it must have a unique structure different from other regular carbons.
Noda and Inagaki model [Nod69] of the structure of the glassy carbon proposes that there is a contribution of both tetrahedral bonds together with trigonal bonds to the structure. The Furukawa model [Fur64] on the other hand proposed that the glassy carbon structure consists of all kinds of C-C bond, i.e., tetrahedral, planar double, linear triple and also conjugated C-C bond. Figure 2 below shows the proposed model for the structure of glassy carbon by Jenkins and Kawamura [Jen71]. Their model was based on the fact that the structure of glassy carbon bears some resemblance to that of a polymer in which the 'fibrils' are very narrow, curved and twisted ribbons of graphitic carbon. The model has been widely accepted but it has some shortcomings. For instance, the structure shown in figure 2 below will be expected to be permeable to gases because of its many conjoined micropores but it is well known that glassy carbon is impermeable [Jen71].

P.J.F Harris studied four commercially available glassy carbon samples in order to investigate if the fullerene-related structures are truly present. The SIGRADUR® G glassy carbon sample used in this research was also studied. The TEM micrograph of the SIGRADUR® G sample is shown in figure 3 below. It was discovered that the sample consists of tightly curled single carbon layers which enclose micropores of the order of 5 nm in diameter [Har04]. These pores were observed to be bounded by faceted or curved graphitic walls typically containing two to four layer planes as can be seen in figure 3 below. Based on the investigation carried out on these four glassy carbon samples (Sigradur K and Sigradur G, supplied by Hochtemperatur-Werkstoffe GmbH, Germany, and GL-100 and GL-200, supplied by Toyo Tanso, Japan), it was concluded that glassy carbon structure contains certain features which all suggest that it has a fullerene-

related structure. Some of the features contained in the glassy carbon are: faceted structure, completely closed particles, negatively curved features[Har04].

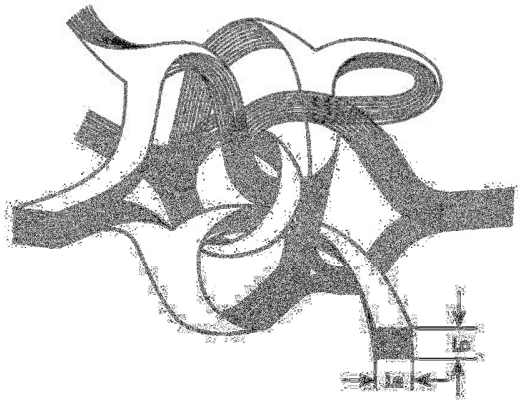

Figure 2: The Jenkins–Kawamura model of glassy carbon. La and Lc are the lengths of the graphitic domains perpendicular and parallel to the graphite c axis [Pie93].

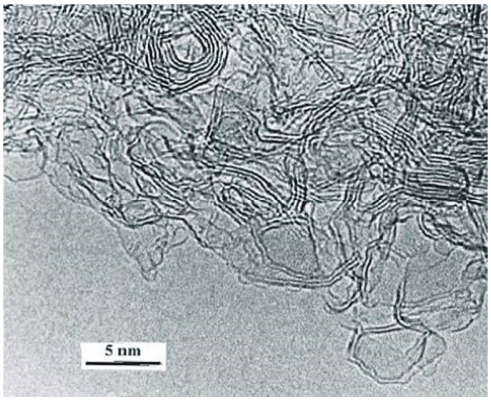

Figure 3: TEM image of SIGRADUR®G glassy carbon [Htw06].

The structure of glassy carbon includes both graphitic (sp^2) and diamond (sp^3) bonds. This perhaps contributes to the isotropy, high hardness and strength of the material.

The structure of glassy carbon will be discussed further in chapter 6 where changes in the structure of glassy carbon as a result of ion implantation and annealing are outlined.

1.4 RESEARCH OBJECTIVES

The scope and objectives of this research is to investigate the following:

i. Investigate if glassy carbon will be a good replacement for stainless steel, nickel alloys and other nuclear waste containers. This was thought to be necessary because of the distinct features of glassy carbon as explained earlier.
ii. The diffusion mechanism of strontium in glassy carbon.
iii. The structural changes of glassy carbon due to strontium ion bombardment and implantation and subsequent heat treatment.
iv. The surface and topography changes of glassy carbon due to ion implantation and heat treatment.

The literature search carried out showed that there has been no report on the diffusion, surface and structural changes of strontium implanted glassy carbon using Rutherford backscattering, Scanning electron microscopy and Raman microscopy.

To investigate these properties, SIGRADUR®G glassy carbon samples were implanted with 2×10^{16} Sr^{+}/cm^{2} at 200 keV at room temperature. The glassy carbon was annealed isochronally from 300 ^{0}C to 900 ^{0}C for one hour.

The analysis of the RBS spectra, Raman spectra and SEM micrographs obtained are discussed in chapter 6.

1.5 REFERENCES

[Bro91] L.R. Brown, C. Flavin, S. Postel, Saving the Planet: How to Shape an Environmentally Stable Global Economy, W.W Norton & Company, New York, 1991.

[Com96] US Nuclear regulatory commission, Radioactive Waste: Production, Storage, Disposal, NRC, Washington, DC, 1996.

[Fur64] K. Furukawa, Nippon Kessho Gakkaishi 6 (1964) 101.

[Har04] P.J.F. Harris, Philosophical Magazine 84 (2004) 3159.

[Hla10] T. T. Hlatshwayo, Diffusion of Silver in 6H-SiC, PhD thesis, University of Pretoria, 2010.

[Htw13] www.htw-germany.com, 1st February, 2013.

[Jen71] G.M. Jenkins, K. Kawamura, Nature 231 (1971) 175.

[Nod69] T. Noda, M. Inagaki, S. Yamada, Bulletin of the Chemical Society of Japan 41 (1969) 3023.

[Pie93] H.O. Pierson, Handbook of Carbon, Graphite, Diamond and Fullerenes, Noyes Publications , New Jersey, 1993.

[Wer92] L. Werme, The Institute of Materials, United Kingdom 1 (1992) 32.

[www1] www.world-nuclear.org, 18th April, 2013.

[www2] www.webelements.com, 18th April, 2013.

[www3] www.wikipedia.org, 16th April, 2013.

[Yim00] M. Yim, K.L. Murty, JOM 52 (2000) 26.

CHAPTER 2

DIFFUSION IN SOLIDS

Atoms in solid materials are constantly vibrating around their lattice positions. An atom with enough thermal energy which is greater than the displacement energy can migrate to an empty lattice site or interstitial site, this action is known as diffusion. Diffusion is a transport phenomenon that largely depends on concentration gradients and it is mostly responsible for the chemical reactions and microstructural changes in solids.

Industrial applications of diffusion include: hardening of steel, doping of semiconductors, oxidation of metals and solid-state formation of compounds etc.

2.1.1 FICK'S FIRST LAW

The expression for the flow of particles from a region of higher concentration to a region of low concentration is similar to that for the flow of heat and it can be expressed in one dimension as [Gup05]:

$$J = -D\frac{\partial C(x,t)}{\partial x} \qquad 2.1$$

Here, C is the concentration of the diffusing material; it is a function of the position x in the sample and the diffusion time t. D is the diffusion coefficient or diffusivity and it relates the flux (J) to the concentration gradient $\left(\frac{\partial C}{\partial x}\right)$ [Gup05]. Equation 2.1 is known as Fick's first law and it was named after A. Fick who first formulated the expression. For an isotropic medium, Fick's first law can be written in three dimensions as [Hei05]:

$$\bar{J} = -D\nabla C \qquad 2.2$$

2.1.2 FICK'S SECOND LAW

In most real life situations where diffusion occurs, both the concentration gradient and concentration profile change with time. These changes modify the Fick's first law and a new law is formulated. The new law known as Fick's second law is derived from equation 2.1 above and the continuity equation.

Considering a cylinder of unit cross sectional area, A. if we take two cross-sections separated by a distance δx as shown in the figure below, J_1 will not be the same as J_2

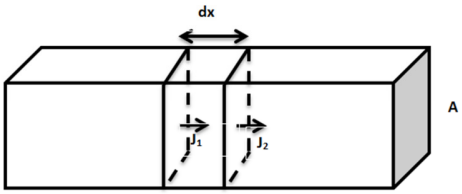

Figure 2.1: A differential volume element in a bar of cross-sectional area A. The flux of the impurity entering and exiting the volume element is given as J_1 and J_2 respectively. [Cam96]

For the long bar shown in Fig. 2.1, with cross section A, if we consider a small volume of length δx with a flux of J_1 entering the volume and a flux of J_2 exiting, we have [Cam96]:

$$\frac{\partial J}{\partial x} = \frac{J_2 - J_1}{dx} \qquad 2.3$$

If $J_1 \neq J_2$, the concentration of the diffusing element in the bar must change. Since the number of impurities in the volume element is the product of the concentration and differential volume element (A.dx), then the continuity equation can be written as:

$$A.\,dx\,\frac{\partial C}{\partial t} = -A(J_2 - J_1) = -A.\,dx\frac{\partial J}{\partial x} \qquad 2.4$$

Equation 2.4 can also be written as:

$$\frac{\partial C(x,t)}{\partial t} = -\frac{\partial J}{\partial x} \qquad 2.5$$

Substituting equation 2.1 for 'J' in equation 2.5, we have:

$$\frac{\partial C(x,t)}{\partial t} = \frac{\partial}{\partial x}\left(D\frac{\partial C}{\partial x}\right) \qquad 2.6$$

Equation 2.6 is the generalized form of Fick's second law. If the diffusion coefficient is assumed to be independent of position, then the equation above is reduced to:

$$\frac{\partial C(x,t)}{\partial t} = D\frac{\partial^2 C(x,t)}{\partial x^2} \qquad 2.7$$

The Fick's second law can also be expressed in three dimensions for an isotropic medium as:

$$\frac{\partial C}{\partial t} = D\nabla^2 C \qquad 2.8$$

In a limited temperature range, the temperature dependence of diffusion coefficient is given by Arrhenius equation as:

$$D = D_0 \exp\left(-\frac{E_A}{kT}\right) \qquad 2.9$$

where E_A is the activation energy, k is the Boltzmann's constant, D_0 is a temperature independent factor and T is the temperature in Kelvin.

2.2 TYPES OF DIFFUSION COEFFICIENTS

It is important to distinguish between diffusion coefficients and mechanisms of diffusion. Self-diffusion coefficient and interdiffusion coefficients will be briefly explained in this section.

2.2.1 SELF-DIFFUSION COEFFICIENT

The motion of atoms in a lattice is a random process; it therefore results in local displacement of individual atoms [Mit12]. This random-walk movement of atoms hopping from one lattice site to a next one is referred to as self-diffusion. Self-diffusion generally takes place in the absence of concentration gradient [Mur01]. Because there is no concentration gradient, the diffusivity, which often depends on chemical composition of the system, is assumed to be constant [Zha10]

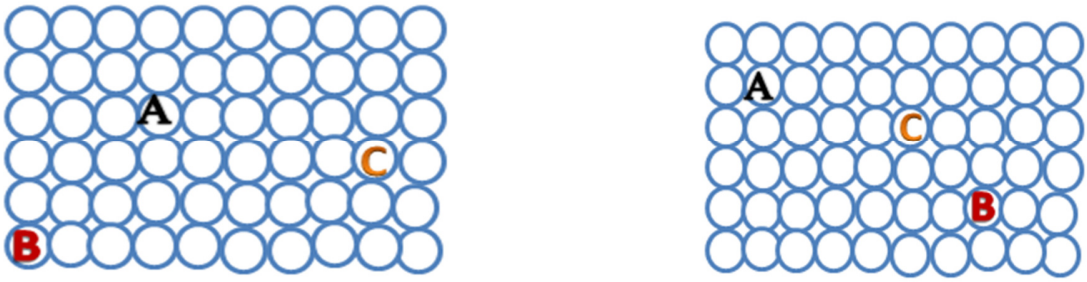

(a) (b)

Figure 2.2: An illustration of the change in the positions of atoms in a solid before and after self-diffusion

2.2.2 INTERDIFFUSION OR CHEMICAL DIFFUSION

If we have a mixture of solids i.e. an alloy consisting of materials X and Y, the atoms from X begin to enter Y and vice versa. This "mixing" is known as interdiffusion or chemical diffusion. The latter name originates from the chemical potential gradient which exists and which is the "driving force" for the diffusion. The mixing continues until the atoms are completely evenly distributed [Npt12].

(a) (b)

Figure 2.3: The diagram illustrates the "mixing" of atoms during interdiffusion.

2.3 MECHANISMS OF DIFFUSION IN SOLIDS

The mechanisms of diffusion in solids are largely connected with defects. The presence of point defects such as vacancies or interstitials often result in diffusion. In this section, the three most common mechanisms of diffusion, viz. vacancy, interstitial and interstitialcy diffusion will be discussed.

2.3.1 VACANCY MECHANISM

In the presence of vacancies i.e. vacant lattice sites, an atom can interchange from its lattice site to an adjacent unoccupied lattice site. Usually, the energy required for an atom to break its bond and move to a vacant lattice site is less because atoms next to vacant site are bonded to fewer atoms as a result of the displacement of one of the lattice atom.

(a)

Figure 2.4: A schematic illustration of the vacancy diffusion mechanism: (a) and (b) are the positions of the atom before and after diffusion respectively

2.3.2 INTERSTITIAL MECHANISM

In solids containing impurities, small atoms of impurity elements such as carbon and nitrogen are usually incorporated in the interstitial sites of such solid. These atoms can jump from one interstitial site to the other; this is known as interstitial mechanism.

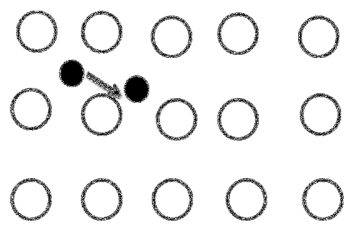

Figure 2.5: Interstitial mechanism of diffusion

2.3.3 INTERSTITIALCY MECHANISM

In the interstitialcy mechanism, self-interstitials i.e. extra atoms located between lattice sites push a neighbouring atom into an interstitial position and occupies the lattice site of the displaced neighbour. Unlike in interstitial mechanism, the self-interstitials are usually the same size as the atoms located in the lattice sites [Hei05].

(a) (b)

Figure 2.6: Interstitialcy mechanism of diffusion: (a) and (b) are the positions of the self-interstitial before and after diffusion respectively.

2.4 REFERENCES

[Cam96] S.A. Campbell, The Science and Engineering of Microelectronic Fabrication, Oxford University Press, New York, 1996.

[Gup05] D. Gupta, Diffusion Processes in Advanced Technological Materials, William Andrew, New York, 2005.

[Hei05] P. Heitjans, J. Kärger, Diffusion in Condensed Matter, Springer, Berlin, 2005.

[Npt12] www.nptel.iitm.ac.in, 25th October 2012.

[Mit12] www.mit.edu, 24th October, 2012.

[Mur01] G.E. Murch, Phase Transformations in Materials, Wiley-VCH, Weinheim, 2001.

[Zha10] Y. Zhang, Reviews in Mineralogy and Geochemistry 72 (2010) 5.

CHAPTER 3

ION IMPLANTATION

Impurities are introduced into materials to improve their physical and electronic properties. This can be done either by thermal diffusion where the substrate is immersed into an atmosphere of vaporized impurity atoms within a furnace or by ion implantation where the impurity atoms are ionized and accelerated towards the target to penetrate into the substrate. Over the years, the ion implantation technique has become the accepted method for doping the less common semiconductors because the dopant profile and dosage can be controlled and monitored.

3.1 CONCEPT OF ION IMPLANTATION

In ion implantation, a beam of positive or negative ions is ionized and accelerated by means of intense electrical fields towards a substrate. The ions then come to rest in the material after all their energies have been lost through elastic and inelastic collisions with the substrate atoms. An impurity ion is said to have been implanted in a substrate when all its energy has been lost to the substrate material. The choice of the implantation energy of the impurity ions is dependent on the substrate material and on the desired depth at which the impurity must be inside the substrate and the application [Cit12].

In this research, 2×10^{16} Sr^{+}/cm^{2} were implanted in glassy carbon with an energy of 200 keV at room temperature. Isochronal annealing was carried out on the implanted glassy carbon to activate possible diffusion of the impurity atoms and also to reduce damages due to implantation.

In order to understand ion implantation, the important processes that occur during ion implantation will be discussed in this chapter.

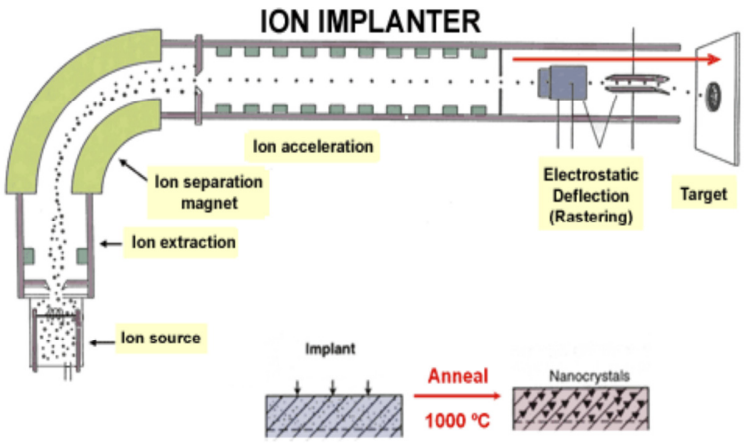

Figure 3.1: Schematic diagram of ion implantation [Van12].

3.2 ION STOPPING

The final distribution and the amount of defects caused by an incident impurity ion are determined by the stopping power, dE/dx of the incident ion. E is the ion energy and x is the distance measured along the direction of the incident ions.

An incident ion loses energy via two ways; nuclear energy loss and electronic energy loss. The energy losses due to nuclear and electronic interactions are correlated since both processes are taking place in close collisions, however, it is justifiable to ignore these correlations and regard electronic stopping as a continuous process separated from nuclear stopping [Dea73]. Therefore, nuclear and electronic stopping are treated like they are independent of each other. Consequently, the total stopping power S of a target, defined by the energy loss (E) per unit path length (x) of the incident ion is the sum of both the nuclear and electronic stopping and it is given as:

$$S = \left(\frac{dE}{dx}\right)_{nuclear} + \left(\frac{dE}{dx}\right)_{electronic} \qquad 3.1$$

The stopping cross section can be derived by dividing S by the target density N´ and then we have:

$$\varepsilon = -\frac{dE}{N'dx} \qquad 3.2$$

where ε is the stopping cross section.

Stopping power is highly dependent of the energy E of the incident ion. This is illustrated in the figure below.

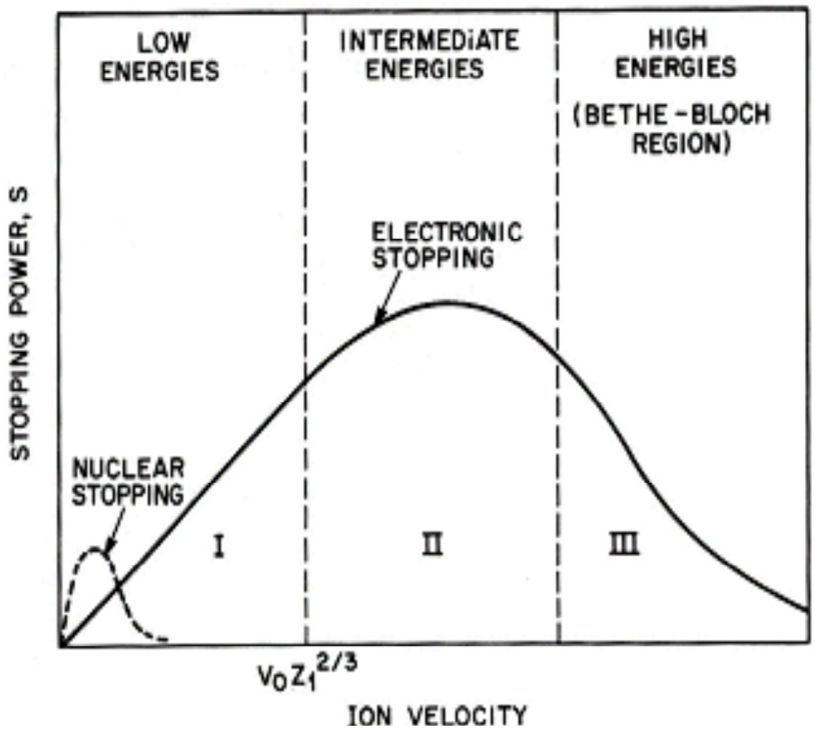

Figure 3.2: Nuclear and electronic components of the ion stopping power as a function of ion velocity. The quantity V_0 is the Bohr velocity given as $\frac{q^2}{4\pi\epsilon_0\hbar}$ and Z_1 is the ion atomic number[Ece12].

It can be seen from the figure above that both processes increase with energy, reach a maximum and then decline again. At low energies, nuclear stopping dominates while electronic stopping dominates at both intermediate and high energies.

3.2.1 NUCLEAR STOPPING

Nuclear stopping is as a result of collisions between two atoms and can be described by classical mechanics. Nuclear scattering can be described by the potential between the incident ion and the target nuclei. If the separation between the incident ion and the target is given as r, then the columbic potential is given as [Cit12]:

$$V_c\,(r) = \frac{q^2 Z_1 Z_2}{4\pi\epsilon_0 r} \qquad 3.3$$

where Z_1 and Z_2 are the atomic number of the implanted ion and the target atoms respectively, ε_0 is the permittivity of free space and q is the electron charge. The electron screens the charge of the nucleus and a screening effect function, $f_s(r)$, must be included, i.e.

$$V(r) = V_c\,(r)\, f_s(r) \qquad 3.4$$

The figure below illustrates a two-body scattering process between an ion and a target atom. An ion of mass M_1 is deflected by the target atom of mass M_2. The position of M_2 relative to M_1 trajectory is the impact parameter represented by P as shown in the figure below. Kinetic energy T is transferred from M_1 to M_2. The value of T can be calculated using the laws of conservation of energy and momentum. It can be written as:

$$T = \frac{4M_1M_2}{(M_1+M_2)^2} E_1 \sin^2\left\{\frac{\theta_2}{2}\right\} \qquad 3.5$$

E_1 is the energy of the projectile with mass M_1 and θ_2 is the recoiling angle. If the maximum possible kinetic energy transfer in a collision is given as T_{max} and there are N target atoms per

unit volume, then the rate of energy loss to nuclear collisions per unit path length is given by [Cit12] as:

$$S_n = \left(\frac{dE}{dx}\right)_{nuclear} = N\int_0^{T_{max}} T d\sigma \qquad 3.6$$

where dσ is the differential cross section.

Nuclear stopping is the result of elastic collisions with the nuclei of the target; therefore, the energy lost by the impurity ion is transferred to the target atom that is recoiled away from its lattice site, creating a defect site. Nuclear stopping is responsible for most of the damage in crystals due to ion implantation.

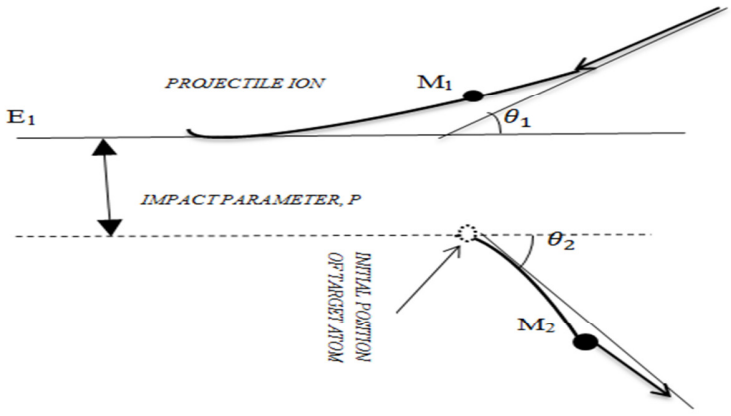

Figure 3.3: A typical two-body scattering process with an impact parameter, p.

3.2.2 ELECTRONIC STOPPING

Electronic stopping is the result of the interactions between an incoming impurity ion and the electrons in the target. The concept of electronic stopping is rather complex compared to nuclear stopping. The complexity of electronic stopping is apparent when the different possible origins are considered. Some of the origins are: direct kinetic energy transfers to target atoms mainly due to electron-electron collisions, excitation or ionization of target atoms, excitation of band electrons, the excitation and ionization of the incident ion itself [Zie85]. Electronic energy loss is difficult to describe using a single theory.

An ion has a high probability of being fully stripped of its electrons at velocities greater than $v = Z_1 e^2/\hbar$. The theory of energy loss under these circumstances derives from the works of Bohr (1913), Bethe (1930) and Bloch (1933); they showed that the stopping power for an ion of velocity v and atomic number Z_1 can be written as:

$$-{}^{dE}/_{dx} = 4\pi {Z_1}^2 e^4 NB/mv^2 \qquad 3.7$$

where m is the electronic mass, N is the number of atoms/cm^3 and B is a dimensionless 'stopping power' parameter [Dea73]. Bethe (1930) deduced that B can be expressed as:

$$B = Z_2 \ln\left({}^{2mv^2}/_{I}\right) \qquad 3.8$$

where Z_2 is the target's atomic mass and I is the mean excitation energy. Bloch (1933) later made corrections and showed that I is directly proportional to the atomic mass of the target:

$$I = kZ_2 \; ; \quad \text{where} \quad k \approx 11eV \qquad 3.9$$

The Lindhard's particle-plasma interaction theory can also be used to estimate the electronic stopping power at low and intermediate levels. The electronic stopping of a charged particle in the local density approximation is given by Lindhard as [Zie85]:

$$S_e = \int I(v,\rho)\, Z_1^2\, \rho\, dV \qquad 3.10$$

The stopping interaction function I in equation 3.10 above is expressed as:

$$I = \frac{4\pi e^4}{mv^2} \cdot \frac{i}{\pi\omega_0^2} \int_0^{\infty} \frac{dk}{k} \int_{-kv}^{kv} \omega d\omega \left[\frac{1}{\varepsilon^{l}(k,\omega)} - 1\right] \qquad 3.11$$

where S_e is the electronic stopping cross-section; I is the stopping interaction function of a particle of unit charge with velocity,v, with a free electron gas density, ρ; Z_1 is the charge of the impinging particle, ρ is the electronic density of the target [Zie85].

The Lindhard model makes the following assumptions:

a. The free electron gas consists of electrons at zero temperature
b. The initial electron gas is of constant density
c. The interaction of the charged particle is a perturbation on the electron gas.
d. All particles are non-relativistic

In this research, strontium ions were implanted in glassy carbon at energy of 200 keV which is within the low energy regime and analysis were carried out using Rutherford backscattering spectroscopy using alpha particles with energy of 1600 keV which is within the intermediate energy regime. The Bohr's theory was used in calculating the stopping power in this research.

3.3 ENERGY STRAGGLING

An energetic incident ion loses energy via many random encounters when it penetrates a target atom and this result in statistical fluctuations in the number of collision processes. Identical energetic particles with the same initial velocity will not have exactly the same energy after passing through a thickness Δx of a homogeneous material. This phenomenon is known as

energy straggling [Chu78]. In material analysis with ion beams, straggling broadens the measured resonance in a nuclear reaction. In this research, the effect of energy straggling is not prominent because our profiles are broad.

Several theories have been used to describe the straggling phenomenon; however, the simplest form is the Bohr's theory. The Bohr's theory states that:

$$\Omega_B^2 = 4\pi Z_1^2 Z_2 e^4 N \Delta R \qquad 3.12$$

where Ω_B is Bohr's energy straggling, which is the standard deviation of the energy broadening. Z_1 and Z_2 are the atomic numbers of the projectile and the target; N is the atomic density and ΔR is the thickness of the target [May77]. The Bohr's theory was derived based on the assumption that:

i. The target atoms are randomly distributed.
ii. The energy loss during a single interaction is very much less than the total energy loss over the entire path.
iii. The projectile velocity is much greater than the orbital electron velocity of the target atoms [Har73].

The third assumption breaks down at low and medium energies.

The Bohr's theory was modified by Lindhard and Scharff [Lin54] alongside Bonderup and Hvelplund [Bon71]. Due to the fact that energy straggling plays only very minor role in our results, the corrections to the Bohr straggling theory is not further discussed.

3.4 RANGE AND RANGE STRAGGLING

Having defined the energy loss of an incident particle moving through a target material as:

$$\frac{dE}{dx} = -S \qquad 3.14$$

where 'S' (the total stopping power) is the sum of the nuclear and electronic stopping respectively.

The mean penetrated path length R which is the average distance the incident ions will travel before finally coming to rest in a target material can be calculated by integrating the energy loss

$$R = \int_0^E \frac{dE'}{N S} = \int_0^E \frac{dE'}{\sum_i(-dE/dx)} \qquad 3.15$$

Due to ion scattering, the ion range normal to the surface is known as the mean projected range R_p. Due to scattering of the ions in their interactions with the substrate atoms, 'R_p' is smaller than the mean total range 'R' .The ions will also be deviated from their initial direction due to the multiple collisions with the substrate atoms and this together with the probability related to the collisions between the ions and the substrate electrons and atoms will result to a lateral spreading i.e. range (and also a projected range straggling ΔR_p) straggling ΔR of the ion beam in the target [Tow06]. Because of the range straggling effect, the impurity profile is approximately Gaussian. The concentration of impurity ions implanted at low energy to a fluence of φ at a depth x in a substrate of atomic density N is related to R_p and ΔR_p and it is given as [Tow06] :

$$C(x) = \frac{\varphi}{\sqrt{2\pi N \Delta R_p}} e^{\left[\frac{-(x-R_p)^2}{2\pi \Delta R_p{}^2}\right]} \qquad 3.16$$

Figure 3.4 shows the final distribution of the implanted strontium ions as a function of distance in the target. The R_p and ΔR_p are also indicated in the Figure.

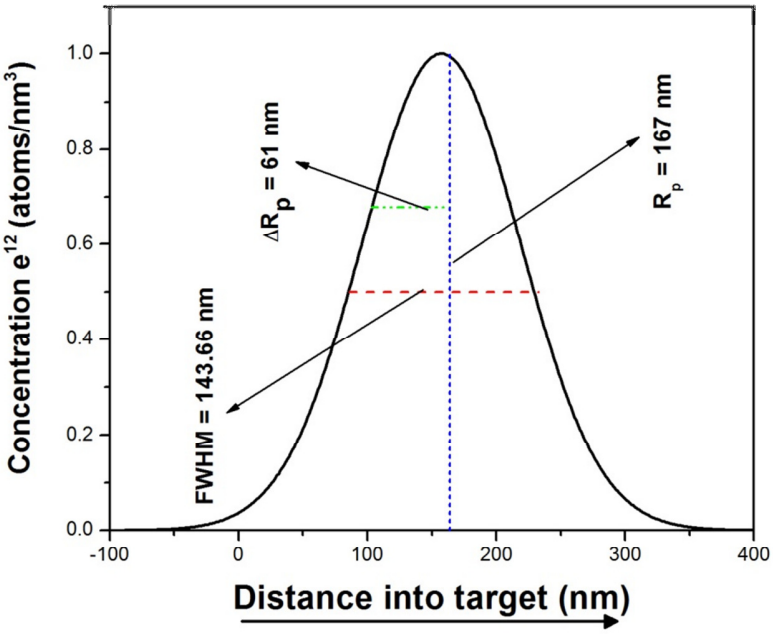

Figure 3.4: Normalized distribution of 200 keV strontium ions in glassy carbon as a function of implantation depth. The projected range ΔR_p, projected range straggling ΔR_p and the full width at half maximum (FWHM) and their values are indicated in the figure.

3.5 REFERENCES

[Bon71] E. Bonderup, P. Hvelplund, Physical Review A 4 (1971) 562.

[Chu78] W.K. Chu, J.W. Mayer, M.A. Nicolet, Backscattering Spectroscopy, Academic Press, New York, 1978.

[Cit12] www.Cityu.edu.hk, 16th October, 2012.

[Dea73] G. Dearnaley, J.H. Freeman, R.S. Nelson, J. Stephen, Defects in Crystalline Solids, Vol. 8, Ion Implantation', North Holland Publishing Co, Amsterdam, 1973.

[Ece12] www.ece.gatech.edu, 22nd October, 2012.

[Har73] J.M. Harris, W.K. Chu, M.-A. Nicolet, Thin Solid Films 19 (1973) 259.

[Lin54] J. Lindhard, M. Scharff, H.E. Schiøtt, Fys. Medd 28 (1954) l954.

[May77] J.W. Mayer, E. Rimini, Ion Beam Handbook for Material Analysis, Academic Press, New York, 1977.

[Tow06] P.D. Townsend, P.J. Chandler, L. Zhang, Optical Effects of Ion Implantation, Cambridge University Press, New York, 2006.

[Van12] www.Vanderbilt.edu, 15th October, 2012.

[Zie85] J.F. Ziegler, J.P. Biersack, Treatise on Heavy-Ion Science 1 (1985) 93.

CHAPTER 4

ANALYTICAL METHODS

4.1 RAMAN SPECTROSCOPY

In 1928, Sir C.V Raman, using sunlight as a source, a telescope as a collector and his eyes as a detector discovered that sunlight can be inelastically scattered to produce patterns that represented different materials. This inelastic scattering of light is named the Raman Effect. Raman Spectroscopy has since then become a powerful and rather excellent technique for identifying molecules and materials. Because of its sensitivity to the microstructure of carbon related materials such as graphite, diamond, glassy carbon etc, it is a precise and efficient technique for the study of lattice dynamics and the vibrational spectroscopy of carbon materials such as graphite and glassy carbon which is the subject of our study [McD94].

From previous studies [McD94] [Wan90] [Nak74] [Tui70a] [Tui70b], Raman spectroscopy has been used to monitor and investigate the effect of ion irradiation and heat treatment on the microstructure of carbon based material. In order to understand Raman spectra of molecules and materials, there is a need to understand the principles of Raman spectroscopy and how it interacts with materials.

Raman Effect occurs when a photon is incident on a molecule. Unlike infrared spectroscopy, an electric dipole is not required for Raman spectroscopy. When light is scattered from a molecule, most of the photons are elastically scattered. Because the scattering of these photons is elastic, they have the same frequency and wavelength as the incident photons [www1]. A small fraction of these incident protons is however scattered at optical frequencies that differs from the frequency of the incident photons. The process leading to this inelastic scattering is termed the Raman Effect [Sha10][www1]. The Raman shift gives information about changes in vibrational, rotational and electronic energy of a molecule or crystal. Usually, Raman spectroscopy is non-destructive but it can become destructive and eventually burn a material if too much laser power

is used. If the laser is focused on a small point for too long, the laser can anneal or damage a sample [www2].

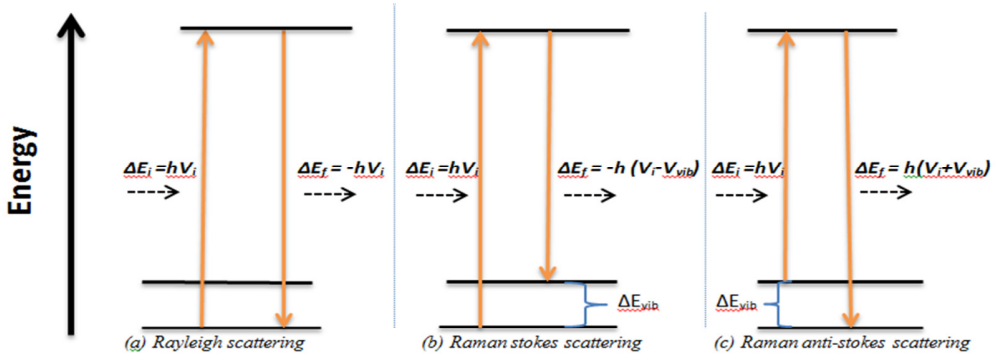

Figure 4.1: Different possible energy diagrams for scattering of photons [www3].

The above figure shows the various energy diagrams when photons are scattered. In Rayleigh scattering (a), there is no exchange or loss of energy, hence, the incident and scattered (emitted) photons have the same energy (elastic scattering). From (b), it can be seen that the atoms or molecules had been excited from their ground state, they absorbed some of the energy and the emitted photon had lesser energy compared to the incident, this Raman interaction is known as Stokes scattering. However, some of these atoms/molecules are already in their excited state as shown in (c), they lose energy to the photon during interaction and the emitted photons have more energy than the absorbed or incident photon, this is termed anti-Stokes scattering [Sha10][Smi05]. The difference between the initial and final state of the scattered photons marked ΔE_{vib} in the diagram above, is vibrational energy measured in Raman spectroscopy. Since different atoms or molecules have varying vibrational energy, ΔE_{vib} because of the difference in molecular structure, it means that different molecules/atoms have different Raman spectra.

A Raman scattering setup consists of an excitation source, a spectrometer, and detector and detection electronics with output devices [Sha10] [Smi05]. The most common source of excitation is a laser. A very monochromatic source of visible light is required to obtain sharp and quality Raman peaks. These laser sources have widths less than 0.1 cm^{-1}, beam divergences less than 1 mrad, and power densities greater than few kW/cm^{2}. The continuous wave (CW) Ar^{+} or

Kr^+ lasers with many discretely tuneable lines in the full visible range are the main sources [Sha10] [McD94]. The major setback of using visible excitation is fluorescence and this is quite common to all visible light spectrometer systems. A Grating spectrometer is used to analyse the scattered photons [Sha10]. The scattered radiation is collected in two ways: using the 90^o scattering geometry or 180^o scattering geometry; in the 90^o scattering geometry, the laser beam is passed through the sample and collected at 90 degrees; this light is then focused into the entrance slit of the Raman spectrometer. In the 180^o system widely used by systems which use a microscope to collect the photons, the laser is delivered through a collection lens and the scattered light is collected back through it [Smi05]. As shown in figure 1, Rayleigh scattering does not produce vibrational energy that can be collected by Raman spectroscopy. It should be noted that because most of the incident photons in spontaneous Raman spectroscopy undergo Rayleigh elastic scattering, it is more intense and dominant than the inelastic Raman scattering. Instruments such as notch filters, tuneable filters, laser stop apertures, double and triple spectrometric systems are used to reduce Rayleigh scattering and obtain high-quality Raman spectra [Sha10] [www1] [Hah07]. The detectors used in Raman spectroscopy have evolved from the human eyes to highly sophisticated instruments. The most commonly used detector nowadays in multi-channelled spectrometer is known as charged coupled devices (CCDs). They detect the incident photon by generation of electron–hole pairs in silicon by a photon of wavelength less than 1100 nm. A typical spectroscopic CCD is made up of 1024 (H) × 256 (V) pixels measuring about 25 × 6 mm. The maximum quantum efficiency for a front-illuminated CCD is about 50%; it can be as high as about 95% for a back-thinned device [Sha10].

As the major interest in this research is to understand the Raman Effect on carbon based material, more precisely glassy carbon, it is of uppermost importance that we understand the Raman spectrum of glassy carbon and other carbon-based material and how they differ from one another.

The identification of diamond by Raman spectroscopy is rather simple and straightforward. The characteristic fingerprint of diamond is a single sharp Raman line located at approximately 1332 cm^{-1}[McD94] [Wan90]. This Raman peak characterizes the sp^3 bonds associated with diamond, and is known as the D peak. In single layered graphite with sp^2 bonds, the D peak is replaced by another Raman peak at ≈ 1575 cm^{-1}, this peak is known as the G peak and it characterizes the sp^2

bonds [Nak74]. However, in polycrystalline graphite, an additional band was recorded at 1355 cm^{-1} and this was attributed to a crystalline size effect [Nak74] [Tui70a][Tui70b].

The first order of the Raman spectrum of glassy carbon consists of a peak at ≈ 1582 cm^{-1} (the G peak) which characterises the sp^2 bonds from the lattice vibration in the plane consisting of the graphite like ribbon in the structure of the glassy carbon [McD94]. An additional peak located at ≈1355 cm^{-1} is also located on the first order of the Raman spectrum. This peak is known as the Raman D peak of the glassy carbon. The D peak is a sort of disorder and it occurs in graphitic materials with small crystallite sizes [McD94]. The Raman spectrum of glassy carbon also consists of an additional peak found in the second order. This peak is known as the D' peak located at ≈ 1615 cm^{-1}, this peak appears just after the G peak. The G and D' peaks are usually unresolved from one another, therefore, the presence of the D' peak in a glassy carbon spectra can lead to a higher than expected G peak position [Fer00].

In this study, the effect of implantation and heat treatment on the structural changes was monitored using Raman spectroscopy. The results and Raman spectrum of the glassy carbon will be shown and explained in detail in chapter 6.

4.2 RUTHERFORD BACKSCATTERING

In Rutherford backscattering (RBS), charged particles like He^+ or H^+ are incident on a target material with energy in the MeV range (1.4 and 1.6 MeV respectively in this research) and the energy of the backscattered ions is recorded and analysed. These charged particles are generated and accelerated in a van de Graaff accelerator; therefore before discussing RBS further, effort will be made to explain how the van de Graaff generator works.

4.2.1 THE VAN DE GRAAFF ACCELERATOR

Rutherford backscattering is a nuclear technique used to analyse the surface of solids. The solid to be analysed is bombarded with alpha particles or protons (usually in the MeV range) and the energy of the backscattered particles is then analysed. These charged particles are generated in an ion source and accelerated to higher energies by building up and maintaining a high potential difference on a spherical conductor. This takes place in an electrostatic generator known as the van de Graaff accelerator. The high voltage generated by the accelerator is maintained by an endless rotating belt which drives the static charges deposited at zero potential to the ion source shell [Gro84]. A schematic diagram of the van de Graaff accelerator is shown in figure 2.

The research reported in this thesis was done using the van de Graaff accelerator present at the University of Pretoria. The maximum energy of this accelerator is 2.7 MeV but energies of 1.4 and 1.6 MeV were used in this study.

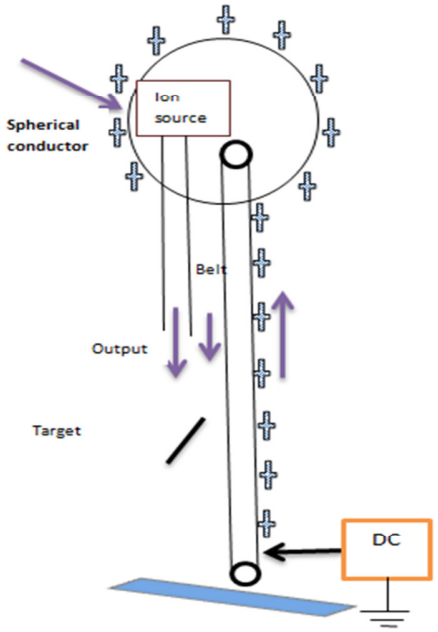

Figure 4.2: A schematic design of a van de Graaff generator [www4]

4.2.2 RUTHERFORD BACKSCATTERING SPECTROSCOPY

The Rutherford backscattering technique was first used in 1913 by Geiger and Marsden to test and prove Rutherford's model of the atom proposed in 1911 [Rut11]. The discoveries made by Rutherford and his students spiked physicists' interest in understanding the nuclear structure. The first real use of RBS was done by nuclear physicists. They discovered using particle accelerators that the backscattering from their target atoms contained 'contaminants' that appeared as a "parasitic effect "in the nuclear reaction particle spectra [Tol49] [Gro84]. In 1967, Surveyor V used an alpha scattering experiment to analyse the composition of the lunar soil [Chu78].

Because RBS is quantitative, simple, has good depth resolution, non-destructive and has good identification power, it has become a popular method for ion beam analysis in thin films. As earlier mentioned, RBS is based on the detection and analysis of backscattered positively charged particles. In this research, a solid state detector was placed at 165^{o} with respect to the incident alpha particles (1.4 and 1.6 MeV respectively) so that only the backscattered particles were detected. A spectrum showing an energy distribution (backscattered yield versus the channel number) was then acquired. The quantitative analysis of all the spectra acquired will be discussed in later chapters. However, a prior knowledge of the basic physical concepts of Rutherford backscattering is needed. In this chapter, the kinematic power (K), scattering cross section (δ) and the depth profiling of a RBS spectrum will be discussed.

4.2.3 KINEMATIC FACTOR (K).

If the collision between the incident particle (alpha particles), M_1 and the stationed target particle of mass M_2 in the figure below is an elastic collision, the elastic collision of the two

masses can be described using the principles of conservation of energy and momentum. From this decription, the energy of the backscattered incident alpha particle is given as [Chu78] :

$$E_1 = KE_o = \left[\frac{M_1\cos\theta \pm \left(M_2{}^2 - M_1{}^2\sin^2\theta\right)^{1/2}}{M_1+M_2}\right]^2 E_o \qquad \textbf{....4.1}$$

E_0 and E_1 are the incident and backscattered energy of the alpha paticles respectively and the ratio of the energy of the incident particle before and after collision is the kinematic factor, K. Equation 4.1 must be adapted if the incident particle travels deeper into the substrate material. The energy of the backscattered alpha particle can be derived if E_o and K is known [Chu78]. When $M_1 \leq M_2$, the plus sign in the equation above holds. When $M_1 \geq M_2$, there will be two solutions for equation 4.1 above, then the incident alpha particles cannot be backscattered. Incident alpha particles of the same energy and incident angle will have varying backscattered energies when they bombard target particles with different masses, hence, the use of Rutherford backscattering to identify the constituents of a sample.

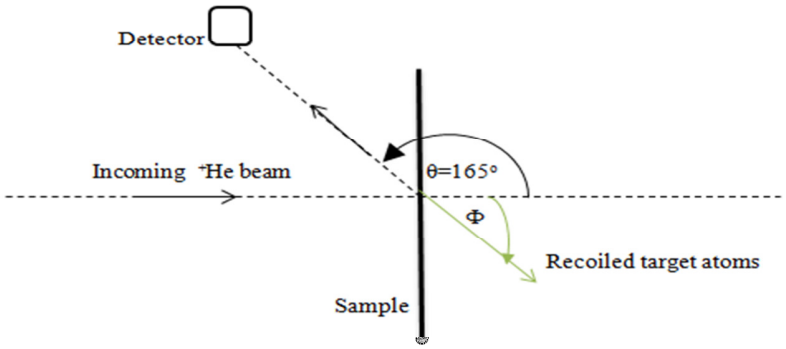

Figure 4.3: Schematic diagram showing the RBS experimental setup at the University of Pretoria [Hla10].

4.3.4 DEPTH SCALING

Depth scaling explains the relationship between the exit (from the substrate) energy E_1 of the alpha particle backscattered at depth x inside the target substrate – see Figure 4.4. The energy of the incident alpha particle in the figure below is given as E_o. The energy E_o reduces to E just before the backscattering because the particle loses energy moving through the substrate. The backscattered particle at depth, x loses more energy on its way out of the target and eventually the energy reduces to the exit energy E_1.

The energy lost by the alpha particle on its way into the target particle is given as $E_o - E$ while the energy lost on its way out is given as $KE_o - E_1$. Assuming that the energy loss $(dE|dx)$ is constant over each path, the energy of the backscattered alpha particle at depth x is then given as [Chu78] [Tes95]:

$$KE_o - E_1 = \left[\frac{K}{\cos\theta_1}\frac{dE}{dx}(in) + \frac{1}{\cos\theta_2}\frac{dE}{dx}(out)\right]x \qquad \textbf{....4.2}$$

The subscripts 'in' and 'out' refer to the constant values along the inward and outward path. KE_o is the energy of the backscattered particles scattered from surface atoms of the target particle.

If ΔE is the energy difference between E_1 and KE_o, then:

$$\Delta E = KE_o - E_1 \qquad \textbf{....4.3}$$

The term $\frac{K}{\cos\theta_1}\frac{dE}{dx}(in) + \frac{1}{\cos\theta_2}\frac{dE}{dx}(out)$ in equation 4.2 above is the backscattering energy loss factor [S]. It gives the relationship between the backscattered energy and depth

Equation 4.2 can be re-written as

$$\Delta E = [S]x \qquad \text{....4.4}$$

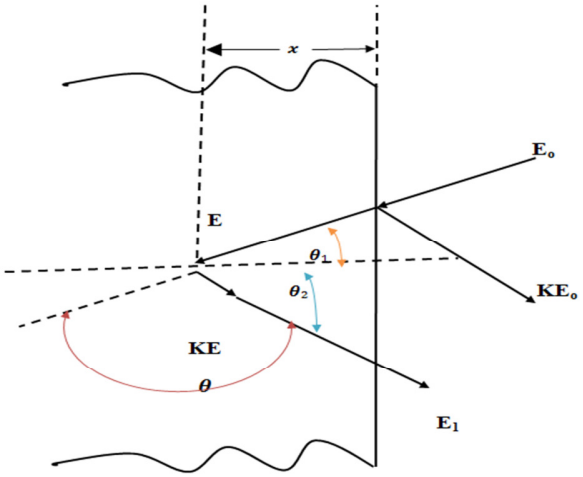

Figure 4.4: a schematic diagram showing the backscattering events in a target consisting of a monoisotopic element [Chu78].

4.3 THE SCANNING ELECTRON MICROSCOPE

The first scanning electron microscope (SEM) was invented in 1931 but it was not recognised as Nobel Prize worthy until 1986 when Ernst Ruska won a Nobel Prize for his contribution in its invention. Perhaps, this was due to the fact that most of the first generation SEM where located in research centres of universities and government agencies [www5]. Electron microscopes were developed due to the limitations of light microscopes which are limited by the physics of light to 500x or 1000x magnification and a resolution of 0.2 micrometres [Vou08].

A scanning electron microscope uses a beam of electrons to form an image of objects on a very fine scale. These electrons are generated by an electron gun which provides a stable beam of electrons of adjustable energy. There are three major types of electron guns: the tungsten filament, Lanthanum hexaboride (LaB_6) and field emission [Haf07].

In this research, a Zeiss Ultra 55 field emission scanning electron microscope was used. This instrument makes use of a field emission electron gun; therefore emphasis will be laid on the field emission guns (FEG). The field emission gun consists of a wire (usually tungsten) of sharp tip with a radius of less than 100 nm. When the electric field at the tip reaches a magnitude of about 10 V/nm, electrons are emitted. A cathode current density of about 10^5 A/cm^2 may be obtained from a field emitter as compared with 3 A/cm^2 from a thermionic source [Hla10] [Gol03].

There are two types of field electron guns; the cold field emitter and the Schottky field emitter. The cold field emitters require ultra-high vacuum conditions (about 10^{-11}) to ensure that the tip is clean and void of contaminants and oxides. The tip is usually flushed (heated for a few seconds) before operation so as to free absorbed gas molecules. The Schottky field emitter uses both heat and nitride coatings to overcome the potential barrier level. The FEGs are better than the tungsten filament and the Lanthanum hexaboride (LaB_6) emission guns because the filaments last longer (due to the cold emission), it produces better resolution and the images produced are brighter. The disadvantages of the FEGs are that a much higher vacuum and a cleaner microscope are required [Dun97].

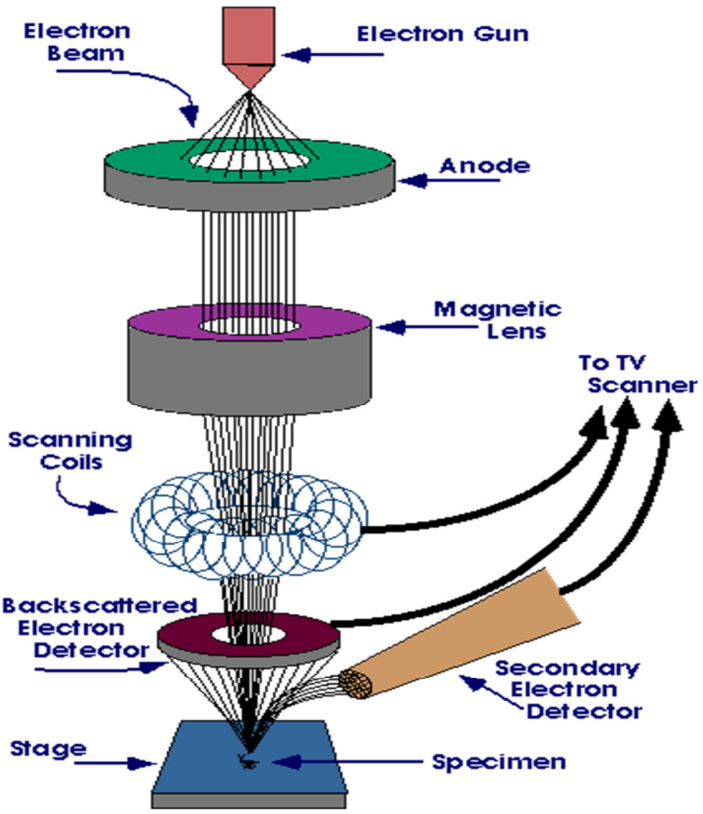

Figure 4.5: Schematic diagram showing how the scanning electron microscope works [www6]

To understand fully how the generation of an electron beam results into an image, we must first understand electron specimen interactions. When an incident electron beam interacts with a sample, the incident electron undergoes two types of scattering - elastic and inelastic scattering. These interactions give rise to various signal events like backscattered electrons, secondary electrons, X-rays, cathode luminescence, specimen current and transmitted electrons. However, for this thesis, only backscattered and secondary electrons will be discussed.

Backscattered electrons are as a result of an elastic collision between an incoming incident beam electron and a target atom. They consist of high-energy electrons that are reflected or back-scattered out of the target sample. Similarly to Rutherford backscattering (as discussed in section 4.1.2) the number of backscattered electrons generated depend on the atomic number of the target. An element with higher atomic number will backscatter more electrons and consequently appear brighter than an element with low atomic number. For instance, gold will appear brighter than carbon because of its higher atomic number. Operating in the backscattered imaging mode

is useful when relative atomic density information in conjunction with topographical information is required [Dun97].

Inelastic collisions between incident electrons and the target gives rise to secondary electrons which again can generate secondary electrons. Secondary electrons have lesser energy (less than 50 eV) compared to backscattered electrons [Haf07]. The signals from secondary electrons are used to study the topography of a sample. Due to their low energy, only secondary electrons that are very near the surface (<10 nm) can exit the sample and be examine, the others are simply absorbed by the sample due to their low energy [Vou08].

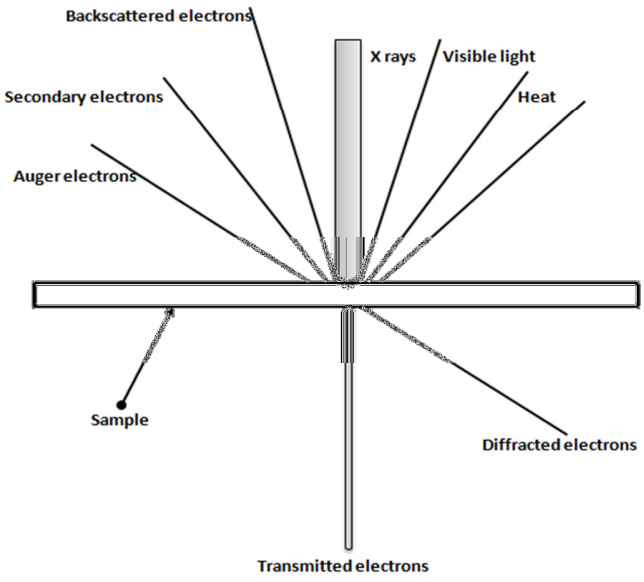

Figure 4.6: A schematic diagram showing the effects of electron bombardment on a target [Vou08].

The overall effect of the elastic and inelastic scattering of these electrons is to distribute the beam electrons over an interaction volume. The dimensions and shape of the interaction volume depends on several factors: the atomic number of the target material, the accelerating voltage and the tilt [Haf07].

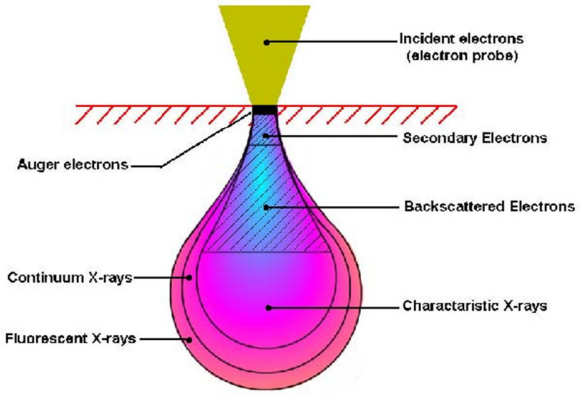

Figure 4.7: Diagram showing electron Beam interaction [www7].

To create a SEM image, the incident electron beam is scanned in a raster pattern across the sample's surface. The emitted electrons are detected for each position in the scanned area by an electron detector. The intensity of the emitted electron signal is displayed as brightness on a cathode ray tube (CRT). By synchronizing the CRT scan to that of the scan of the incident electron beam, the CRT display represents the morphology of the sample surface area scanned by the beam. Magnification of the CRT image is the ratio of the image display size to the sample area scanned by the electron beam [www7].

4.3.1 IN-LENS DETECTOR

The in-lens detector is a high efficiency detector for high resolution secondary electron imaging. It is located above the objective lens and detects electrons directly in the beam path. The detection efficiency of this detector results from its geometric position in the beam path and from the combination with the electromagnetic lens [Zei08].

At an acceleration voltage of maximum 20 kV, the electrons of the primary electron beam are additionally accelerated by 8 kV which is the beam booster voltage. In order to ensure that the electrons reach the specimen surface with the energy set as acceleration voltage, an electrostatic

field is generated at the end of the objective lens by 8 kV. This field acts as acceleration field to the secondary electrons generated on the specimen surface [Zei08].

The electrons hit a scintillator at the in-lens detector and they generate flashlight that is guided out of the beam path by means of a light guide. The light information is multiplied in a photomultiplier and then output as a signal that is then analysed and displayed on the monitor.

The efficiency of the in-lens is dependent on the electric field of the electrostatic lens. This electric field decreases exponentially with distance, therefore, the working distance affects the signal-to-noise ratio of the in-lens detector [Zei08].

The scanning electron microscope can be used to investigate the topography, morphology, composition and crystallographic information of a sample.

In this research, the SEM was used to monitor the surface changes of glassy carbon as a result of strontium ion implantation and heat treatment. The results will be discussed in chapter 6.

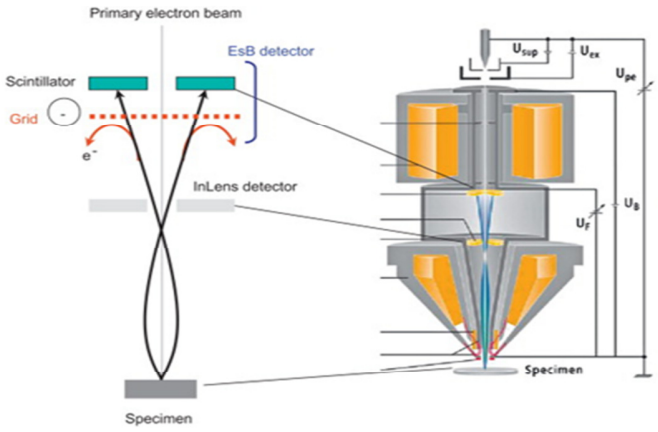

Uex = extractor voltage of first anode

UPE = primary beam voltage

UB = booster voltage

UF = EsB filtering grid voltage

Figure 4.7: Schematics of the in-lens detector[Nag13]

4.4 REFERENCES

[Chu78] W.K. Chu, J.W. Mayer, M.-A. Nicolet, Backscattering Spectroscopy, Academic Press, New York, 1978.

[Dun97] M. Dunlap, J.E. Adaskaveg, Theory, Practice, & Procedures. Facility for Advance Instrumentation. UC Davis 52 (1997).

[Fer00] A.C. Ferrari, J. Robertson, Physical Review B 61 (2000) 14095.

[Gol03] J.I. Goldstein, D.E. Newbury, P. Echlin, D.C. Joy, A.D. Romig, C.E. Lyman, C. Fiori, E. Lifshin, Scanning Electron Microscopy and X-ray Microanalysis, 3rd ed., Springer, New York (2003).

[Gro84] J.J. Grob, P. Siffert, Progress in Crystal Growth and Characterization 8 (1984) 59.

[Haf07] B. Hafner, Characterization Facility, University of Minnesota-Twin Cities (2007).

[Hah07] D.W. Hahn, Department of Mechanical and Aerospace Engineering, University of Florida (2007).

[Hla10] T.T. Hlatshwayo, Diffusion of Silver in 6H-SiC, University of Pretoria, 2010.

[McD94] D.G. McCulloch, S. Prawer, A. Hoffman, Physical Review B 50 (1994) 5905.

[Nag13] M. Nagoshi, T. Aoyama, K. Sato, Ultramicroscopy 124 (2013) 20.

[Nak74] M. Nakamizo, R. Kammereck, P.L. Walker, Carbon 12 (1974) 259.

[Rut11] E. Rutherford, Phil. Mag 21 (1911) 1911.

[Sha10] M. Sharon, Carbon Nanoforms and Applications, McGraw-Hill, Delhi, 2010.

[Smi05] E. Smith, G. Dent, Modern Raman Spectroscopy: a Practical Approach, Wiley, New Jersey, 2005.

[Tes95] J.R. Tesmer, M.A. Nastasi, J.C. Barbour, C.J. Maggiore, J.W. Mayer, Handbook of Modern Ion Beam Materials Analysis, Materials Research Society, Pittsburgh, PA, 1995.

[Tol49] A. V Tollestrup, W.A. Fowler, C.C. Lauritsen, Physical Review 76 (1949) 428.

[Tui70a] F. Tuinstra, J.L. Koenig, The Journal of Chemical Physics 53 (1970) 1126.

[Tui70b] F. Tuinstra, J.L. Koenig, Journal of Composite Materials 4 (1970) 492.

[Vou08] B. Voutou, E.-C. Stefanaki, Physics of Advanced Materials Winter School 1 (2008).

[Wan90] Y. Wang, D.C. Alsmeyer, R.L. McCreery, Chemistry of Materials 2 (1990) 557.

[www1] www.bris.ac.uk, 31st July, 2012.

[www2] www.perkinelmer.com, 31st July, 2012

[www3] www.wikipedia.org, (2013).

[www4] www.ibi.gov, 8th August, 2012

[www5] www.purdue.edu, 20th August, 2012.

[www6] www.herguth.com, 4th April, 2012

[www7] www.mee-inc.com, 25th September, 2013

[Zei08] C.Z.N. GmbH, ULTRA Plus FESEM with Integral Charge Compensator and Embedded AsB and EsB Detectors, 01 ed., Carl Zeiss SMT, Oberkochen, 2008.

CHAPTER 5

EXPERIMENTAL PROCEDURES

50 mm×10 mm SIGRADUR®G glassy carbon samples of thickness 2 mm were implanted with strontium ions. The diffusion behaviour, structural changes and surface modification of the strontium implanted glassy carbon samples were investigated using RBS, Raman spectroscopy and SEM respectively. All experimental procedures and annealing processes will be discussed in this chapter.

5.1 SAMPLE PREPARATION

The samples used for this research were glassy carbon samples from Hochtemperatur-Werkstoffe (HTW), Germany. The company produces both SIGRADUR® G and SIGRADUR® K glassy carbon materials, however, the SIGRADUR® G carbon materials were a preferred choice for this study due to its superiority over SIGRADUR® K materials. Although the SIGRADUR® K materials are relatively denser and harder than the SIGRADUR® G, the SIGRADUR® G carbon materials have higher conductivity, higher corrosion resistance and high temperature resistance.

The samples were mechanically polished on an ATM Saphir 500 polisher with 1µm and 0.25 µm diamond solutions respectively before being cleaned. The samples were placed in an ultrasonic bath and first cleaned in an alkaline soap solution. The samples were then transferred to a new beaker containing de-ionized water. The de-ionized water was used to remove the soap solution from the sample and this was done twice for ten minutes. Methanol was then used to clean the samples for 5 minutes so as to remove the de-ionized water. The samples were dried by blowing nitrogen gas on them for a few minutes and then placed in an oven at 50 ^{o}C for 1h so as to remove volatile impurities on the surface of the carbon samples.

5.2 IMPLANTATION OF STRONTIUM

After cleaning, the samples were implanted with strontium ions by the 400 keV ion implanter Romeo at the Institut für Festkörperphysik, Friedrich-Schiller-Universität Jena, Jena, Germany. The strontium ions were implanted at room temperature at energy of 200 keV with a fluence of 2×10^{16} cm^{-2}. Because of our interest in studying the radiation damage as a result of strontium implantation in glassy carbon, the flux was kept at about 10^{12} ions/cm^2 in order to avoid annealing out of some of the damages due to increase in the substrate material temperature. During implantation the substrate reached a maximum temperature of about 55 °C.

After implantation, the samples were cut into 7 mm×7 mm perfect squares using an Accutom cutter. This was to ensure that the samples fit into sample holders that have been specifically made for RBS and SEM analysis.

To wash off the glue used to fix the samples to the cutter, the samples were again cleaned with acetone, de-ionized water and methanol. This was done in order to remove/prevent contamination.

5.3 ANNEALING OF SAMPLES

Isochronal annealing was employed in this research. The sample was placed in a vacuum tube furnace which anneals up to 1000 °C. A schematic diagram of the annealing equipment is shown in figure 5.1 below. The turbo pump shown in the figure below provides high vacuum (of about 10^{-7} mbar). A thermocouple is placed close to the sample in order to measure and monitor its temperature.

The annealing process was monitored using a computer program shown in figure 5.2. The annealing strip chart gives a clear understanding of the heating up, annealing and cooling down processes. The data acquired from the strip chart was plotted in Figure 5.3 below. The annealing curves shown in Figure 5.3 are for 800 ^{o}C and 900 ^{o}C respectively.

Once the oven has been stabilised at the required annealing temperature, it was dragged over quartz tube until the sample is in the middle of the oven. This step ensured that the sample quickly reached the required temperature. When the annealing period had elapsed, the oven was dragged out and the quartz tube was allowed to cool down to room temperature. The sample was then removed after the fore pump and turbo pump had been turned off and the turbo pump blades have stopped rotating. Usually, it takes about two hours for the turbo pump blades to stop rotating.

The sample was annealed isochronally using the tube furnace. The annealing temperature range was from 300 °C to 900 °C in steps of 100 °C for one hour. RBS, Raman spectroscopy and SEM were used to investigate changes on the sample after every annealing.

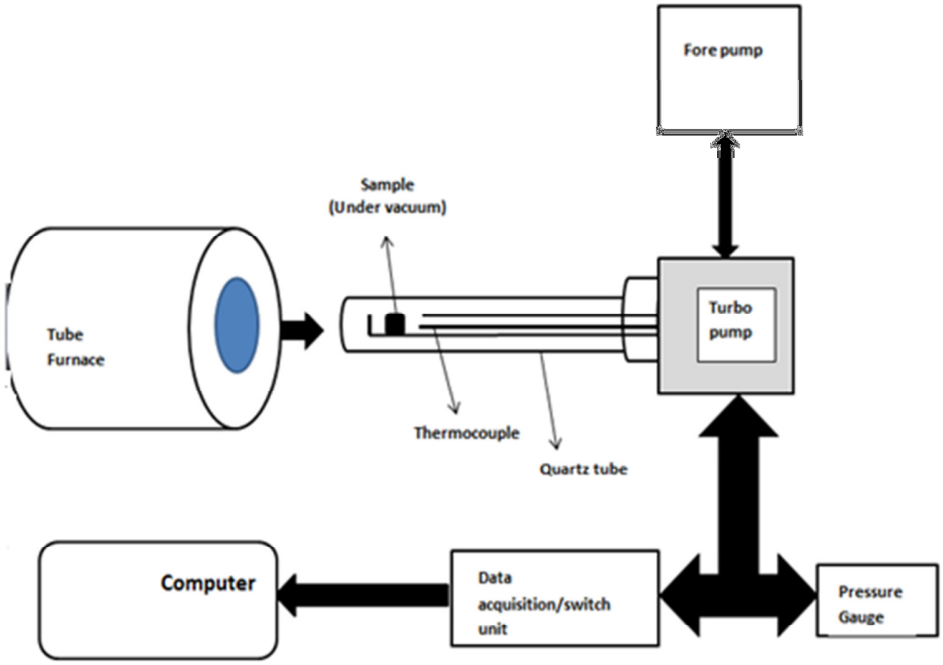

Figure 5.1: Schematic diagram showing the annealing system employed in this research

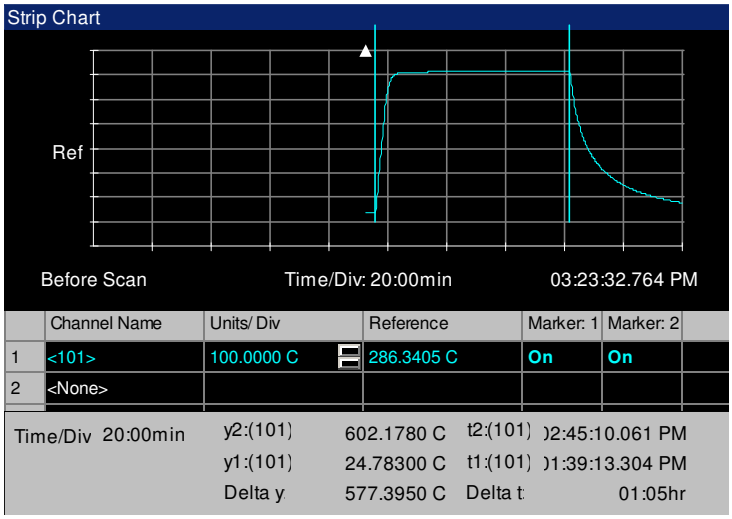

Figure 5.2: Image showing the annealing strip chart of strontium implanted GC annealed at 600^0 for 1h.

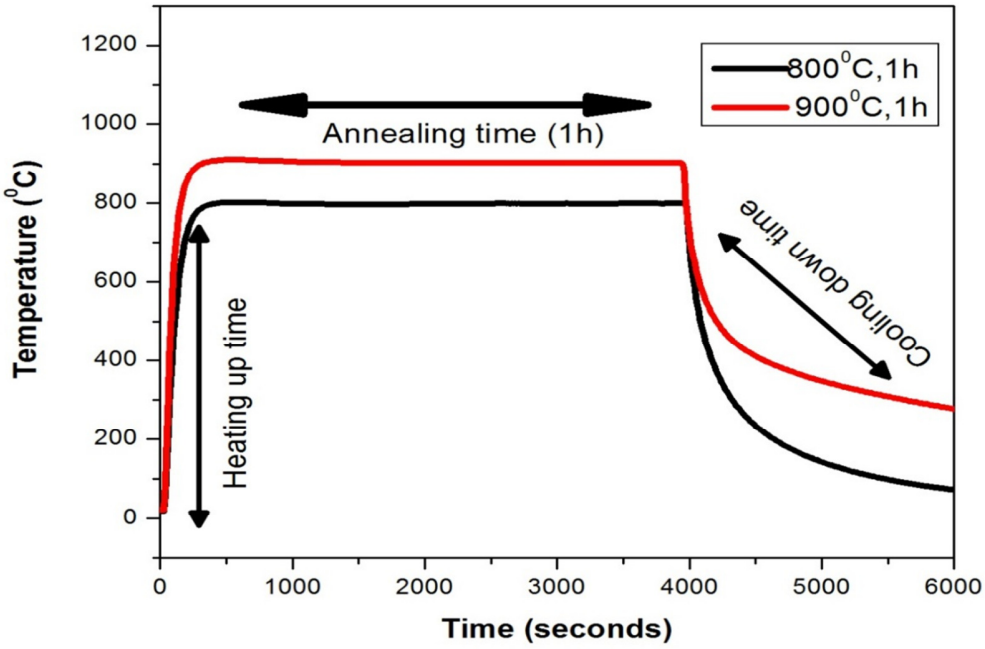

Figure 5.3: Temperature (^{o}C) versus time (seconds).

5.4 MEASUREMENT CONDITIONS

5.4.1 RBS MEASUREMENT CONDITIONS

The strontium implanted glassy carbon samples were analysed using Rutherford backscattering spectroscopy after every annealing. The samples were irradiated with alpha particles of energies 1.4 MeV and 1.6 MeV, respectively, in the Van de Graaff accelerator at the University of Pretoria. A total charge of 8 μC was used throughout this study. Analysing current of 15 nA was used in order to prevent pile up of the backscattered helium particles. Scattering angle of 165^{o} was also employed.

In order to ensure accuracy and noise reductions, repeated readings were taken. For example, a strontium ion implanted glassy carbon sample annealed at 300 ^{o}C for 1h was analysed ten times and an average of the counts was taken. There were no significant changes in the first and last spectrum, indicating that the analysis did not damage the samples.

5.4.2 RAMAN SPECTROSCOPY MEASUREMENT CONDITIONS

The structural changes as a result of ion implantation and annealing were monitored using a Jobin Yvon, Horiba$^{(C)}$ TX64000 Raman spectrometer located at the University of Pretoria. The apparatus consists of a Raman spectrometer with excitation lasers with wavelength ranging from 457.9-641.7 nm and a light microscope with 10×, 50× and 100× magnification objectives. The excitation laser used in this research was an Ar/Kr mixed gas laser (514.6 nm) and the 50× objective was used throughout to ensure uniformity. In order to prevent sample heating, the laser power was kept at ≤ 10 mW at the sample.

The table below shows the conditions used when taking a Raman spectrum in this research.

Incident laser beam (nm)	Laser power (mW)	Eyepiece Magnification	Objective Focus Magnification	Data Range (cm^{-1})
514	**≤ 20**	**10×**	**50×**	**800-1800**

5.4.3 SEM MEASUREMENT CONDITIONS.

Surface modifications of the glassy carbon samples as a result of ion implantation and heat treatment were investigated using the Zeiss Ultra Plus SEM located at the University of Pretoria. An analysing voltage of 2 kV was used throughout this work. In-lens SEM images of the sample were taken before implantation, after implantation and after every heat treatment so as to investigate all surface changes due to these treatments. The working distance was kept between 2.5-3.0 mm and magnifications of 1µm, 10 µm and 200 nm respectively were used and their resulting micrographs were compared.

CHAPTER 6

RESULTS AND DISCUSSIONS

The diffusion mechanism, structural and surface modification of strontium implanted glassy carbon was investigated using Rutherford backscattering spectroscopy, Raman spectroscopy and scanning electron microscopy (SEM) respectively.

Figure 6.1 shows the RBS spectrum of glassy carbon implanted with strontium ions at room temperature. The position of each element depends on the mass and hence, the kinematic factor of each element. If the mass of the target atom M_2 is greater than the mass of the projectile atom M_1, the expression for the kinematic factor can be written in a simplified form as:

$$K_{element} = \left[\frac{(M_2 - M_1)}{(M_2 + M_1)}\right]^2 \qquad 6.1$$

Where $K_{element}$ is the kinematic factor of the element with mass M_2. M_1 is the mass of the incident alpha particle.

Strontium is a heavier element than carbon, therefore, it has a higher kinematic factor value; hence, it appears at higher energy position as compared to carbon. The carbon edge is located at channel number 102 while the strontium edge is located at channel number 421. An additional oxygen peak is observed at channel number 175, it is still unclear why this peaks appeared in all the RBS spectra.

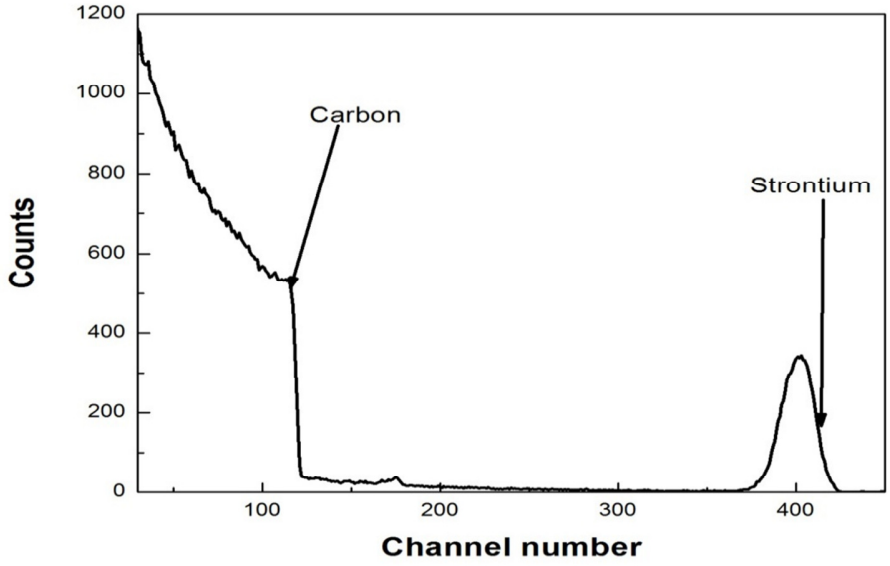

Figure 6.1: RBS spectrum of glassy carbon implanted with strontium at room temperature at a fluence of 2×10^{16} Sr^{+}/cm^{2}

6.1.1 AS-IMPLANTED STRONTIUM DEPTH PROFILE

The strontium distribution shown in Figure 6.1 is approximately Gaussian which is in agreement with a typical ion implantation profile. The strontium profile was fitted with the Genplot computer program and the moments were compared with SRIM 2012 [Zie12] predictions given in Table 6.1. The experimental projected range, R_P was estimated to be about 165 nm while the theoretical value obtained from SRIM 2012 is 157 nm. Although the implanted strontium peak is deeper than the theoretical predictions, the discrepancy is within the experimental error (about 5 %) and within the accuracy of SRIM. The SRIM program has accuracy within 5-10 % error [Zie12].

The straggling, ΔR_P value obtained experimentally is 43 % larger than the value predicted by SRIM12 shown in Table 6.1. The experimental profile is not symmetric and this can be seen from the skewness and kurtosis values shown in Table 6.1. The skewness value of a distribution tells if the peak is symmetric or asymmetric. The skewness value is zero, i.e. $\gamma = 0$, when the peak is symmetric. The skewness (γ) is negative when the distribution is skewed in front of R_P

or positive when the distribution is skewed behind R_P. The experimental profile skewness value is -0.238. This negative value implies that the strontium peak is skewed in front of Rp, this can be seen in Figure 6.2. This implies also that redistribution of strontium is already taking place even during implantation.

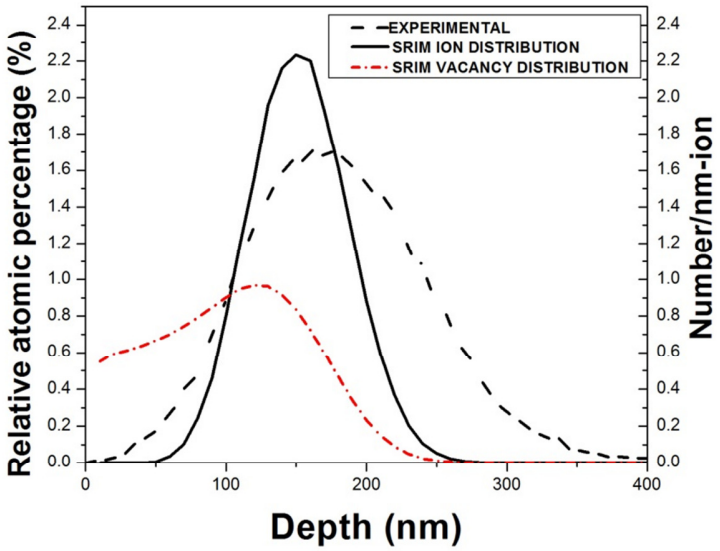

Figure 6.2: RBS depth profile of strontium implanted glassy carbon compared with SRIM 2012 predictions.

The kurtosis (β) values obtained from SRIM12 and experimentally also agree with an approximately Gaussian distribution.

Figure 6.2 shows the number of vacancies produced as a result of implantation of strontium in glassy carbon as predicted by SRIM12. It can be seen from the SRIM12 predictions that a large number of atoms were displaced on the surface of the glassy carbon. This perhaps explains the migration of the implanted strontium towards the surface of the glassy carbon after heat treatment. One can say that the diffusion of the implanted strontium was induced by radiation damage.

The difference between the straggling, ΔR_P, obtained from SRIM12 and the experimental data is due to the fact that diffusion of strontium was already taking place during implantation. This diffusion of strontium was induced by irradiation of the sample during implantation.

The differences in the moments were also caused by the approximations made by the SRIM12 program when simulating the interactions between the incident ions and the substrate atoms. The assumptions made by the SRIM12 program include:

1. The SRIM program does not take the crystallinity of the substrate into consideration i.e. it assumes that the substrate is amorphous.
2. The predictions of the projected range are based on binary collisions alone (Effects of neighboring atoms are neglected).
3. The electronic and nuclear stopping powers are an averaging fit to a large number of experiments.
4. The recombination of interstitials with vacancies is neglected. The electronic and nuclear stopping powers are an averaging fit to a large number of experiments.

Table 6.1: Table showing the comparisons between the experimental data and the theoretical data acquired from SRIM 2012.

	EXPERIMENTAL	SRIM
PROJECTED RANGE	165.17	157.3
STRAGGLE	61	34.5
SKEWNESS	-0.238	0.015
KURTOSIS	2.6	3

6.1.2 ISOCHRONAL ANNEALING RESULTS.

The RBS depth profiles of the implanted strontium before and after heat treatment will be discussed in this section. Sequential isochronal annealing was carried out on the sample for one hour in steps of 100 ^{o}C.

The sample was initially annealed at 200 ^{o}C for one hour but no noticeable change was observed in the strontium peak, as can be seen from Figure 6.3. The strontium depth profile remained the same when compared to the as-implanted profile. This clearly indicates that the temperature was too low to cause any significant change in the strontium distribution, i.e. to cause any diffusion of the strontium at this temperature.

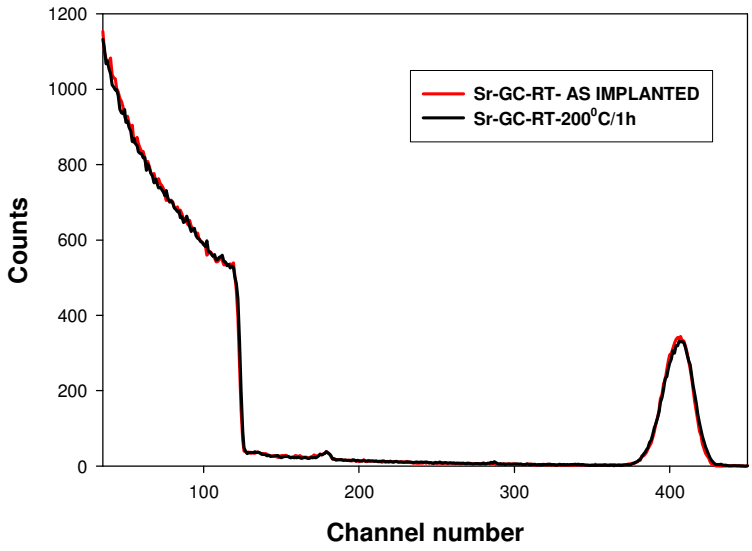

Figure 6.3: RBS spectra of strontium implanted glassy carbon annealed at 200 ^{o}C for 1hr compared to the as-implanted profile.

When the annealing temperature was increased to 300 ^{o}C, diffusion of strontium into the bulk and towards the surface of the glassy carbon was observed as shown in Figure 6.4 below. From Figure 6.4, it can be seen that strontium peak became broader (although still Gaussian) when compared to the as-implanted profile. There was no significant (i.e. within the experimental error) loss of strontium from the sample at this temperature despite the redistribution of the

strontium. The diffusion mechanism that occurred at this temperature is Fickian diffusion i.e. it obeys Fick's laws.

As seen in Figure 6.4 below, after annealing the sample at 400 ^{o}C, further diffusion of strontium towards the surface of the glassy carbon substrate was observed. There was no further migration of strontium into the bulk of the substrate. The diffusion of strontium after annealing at this temperature was also accompanied by segregation of strontium on the surface of the substrate and the strontium depth profile was no longer Gaussian. The accompanying segregation of strontium on the surface of the glassy carbon depends largely on Gibbs free energy.

The sample was further annealed from 500 ^{o}C – 600 ^{o}C as shown in Figure 6.4. Further migration of strontium towards the surface of the glassy carbon was observed. This diffusion was also accompanied with segregation of strontium on the surface. It was also observed that the intensity of the strontium peak formed on the surface became higher with increasing annealing temperature. The strontium depth profiles at these temperatures were not Gaussian.

The intensity of the segregated strontium peak was very high after annealing the sample at 700 ^{o}C. This was due to the fact that this annealing temperature is still lower than the melting point of strontium (~769 ^{o}C). As seen if Figure 6.5, there was no loss of the segregated strontium at this temperature.

As can be seen from Figure 6.4, when the sample was annealed at 800 ^{o}C and 900 ^{o}C which are temperatures higher than the melting point of strontium (~769 ^{o}C), the segregated strontium began to evaporate and huge loss of strontium was observed with about 30 % strontium ion being retained.

Figure 6.5 shows the retained strontium after heat treatment at various temperatures. After annealing the glassy carbon from 300 ^{o}C – 700 ^{o}C, which are temperatures lower than the melting point of strontium, no strontium (within the experimental error) was lost. However, after annealing the sample at 800 ^{o}C and 900 ^{o}C respectively, significant loss of strontium was observed with less than 30 % of the strontium retained at 900 ^{o}C.

The above results are in agreement with the work done by D.F. Langa *et al.* [Lan12]. In their research, cesium ions were implanted in glassy carbon at energy of 360 keV to a fluence of 2×10^{16} Cs^{+}/cm^{2}. This implantation was done at room temperature, 350 ^{o}C and 600 ^{o}C respectively. The room temperature implanted sample was annealed isochronally for 1 hour in vacuum from 200 ^{o}C – 600 ^{o}C. They found that diffusion of Cs towards the surface of the glassy carbon substrate was already taking place at room temperature. This diffusion was enhanced at 350 ^{o}C and 600 ^{o}C respectively. Segregation of Cs on the surface of the glassy carbon was also observed for the 600 ^{o}C implanted sample. The sample implanted at room temperature was isochronally annealed for 1 hour in steps of 100 ^{o}C. Surface and bulk diffusion of Cs were observed after heat treatment. The surface diffusion was accompanied with segregation and subsequent evaporation of Cs. The significant difference between the acquired results by D.F Langa *et al.* and the experiments done in this research is that loss of Cs was already observed at 200 ^{o}C. This is because of the low melting point of Cs (29 ^{o}C) when compared to strontium (769 ^{o}C). 72 % of the implanted Cs was already lost after heat treatment at 600 ^{o}C.

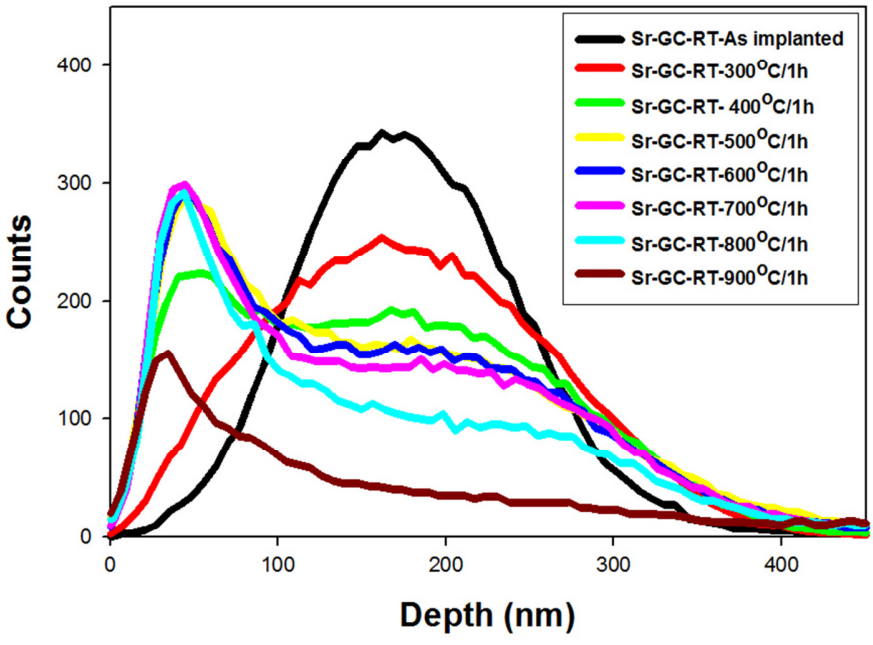

Figure 6.4: RBS depth profile of the implanted strontium distribution after implantation and after annealing at different temperatures.

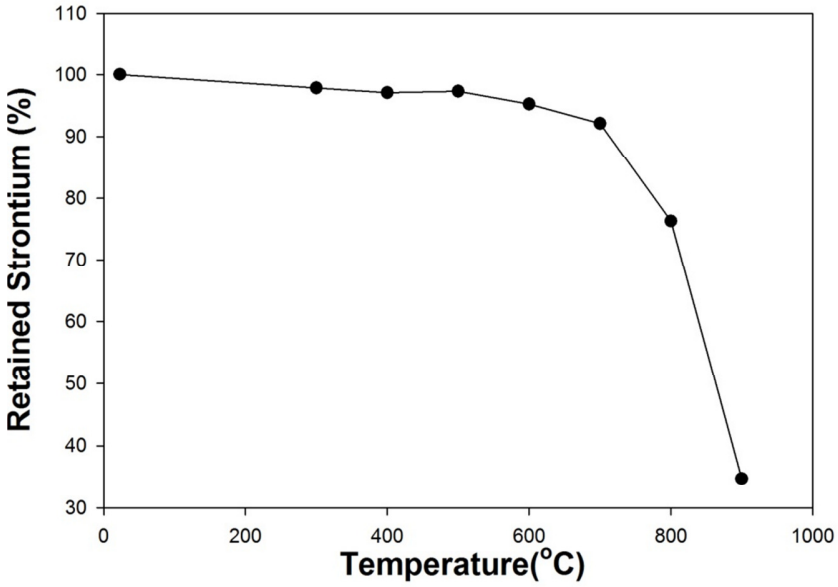

Figure 6.5: Comparison of retained strontium at different annealing temperatures.

6.2 RAMAN SPECTROSCOPY RESULTS

The structural changes of the glassy carbon after annealing and heat treatment were investigated using Raman spectroscopy. Raman spectrum of glassy carbon is shown in Figure 6.6. The spectrum shows the D (disorder) and G (graphite) peaks. The D peak characterizes the sp^3 bond present in the glassy carbon while the G peak characterizes the sp^2 bonds present. The disorder (D) peak present in glassy carbon and other forms of amorphous carbon is also due to a crystalline size effect [McD94]. The D and G peaks and their corresponding peak positions are shown in Figure 6.6 below.

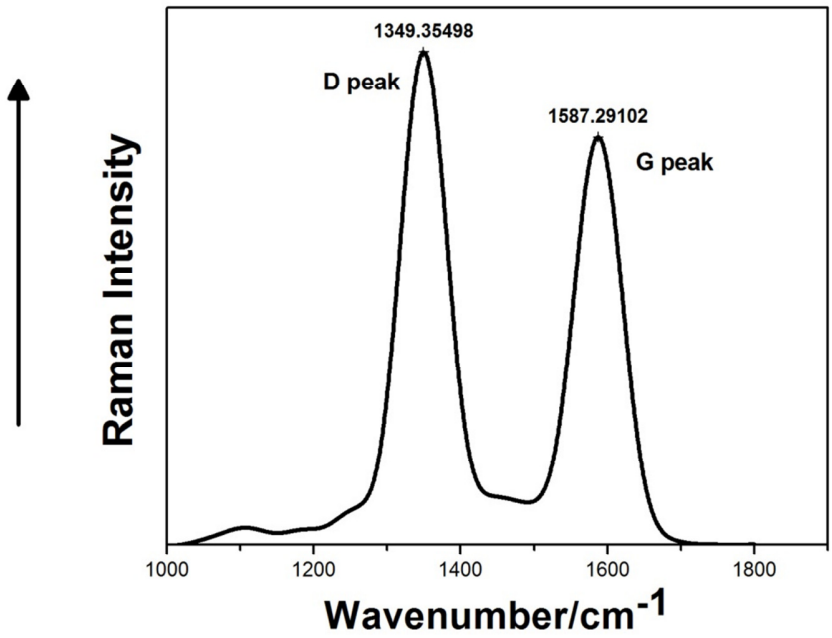

Figure 6.6: Typical Raman spectrum of glassy carbon.

Figure 6.7 shows the Raman spectrum of glassy carbon before and after strontium ion implantation. After the high fluence implantation of strontium, the two Raman peaks (i.e. the D and G peaks) of glassy carbon merged into a single broad band. McCulloch *et al.* [McC94] studied the change in the D and G peaks for Xe^+ bombarded glassy carbon as function of fluence. At the lowest fluence, 5×10^{12} Xe^+ / cm^{-2} there was virtually no change in the peaks. With increasing fluence the two peaks became initially broader and started to merge until they formed a single broad band, which above 5×10^{15} Xe^+ / cm^{-2} exhibited no further changes. TEM investigations showed that the glassy carbon at this fluence (4 dpa) was completely amorphised. During amorphization approximately 15% of the graphitic bonds were converted into sp^3 bonds (diamond-like bonds) accompanied with an increase in density of the implanted layer. The amorphous layer also became more resistant to abrasion than the virgin glassy carbon probably due to the sp^3 bond formation. This development of a broad "damaged" peak between about 1300 cm^{-1} to 1600 cm^{-1} is not particular to glassy carbon it is also observed in other carbons –

see for example [Niw92] and [Niw95]. Niwase [Niw95] found that with increasing He^+ bombardment fluence, the Raman spectrum of HOPG (highly oriented pyrolytic carbon) changed from a single G peak to G and D peaks (due to the displacement of carbon atoms to a position between the graphitic layer and subsequent sp^3 bonding) at low fluences to the single broad band at high fluences.

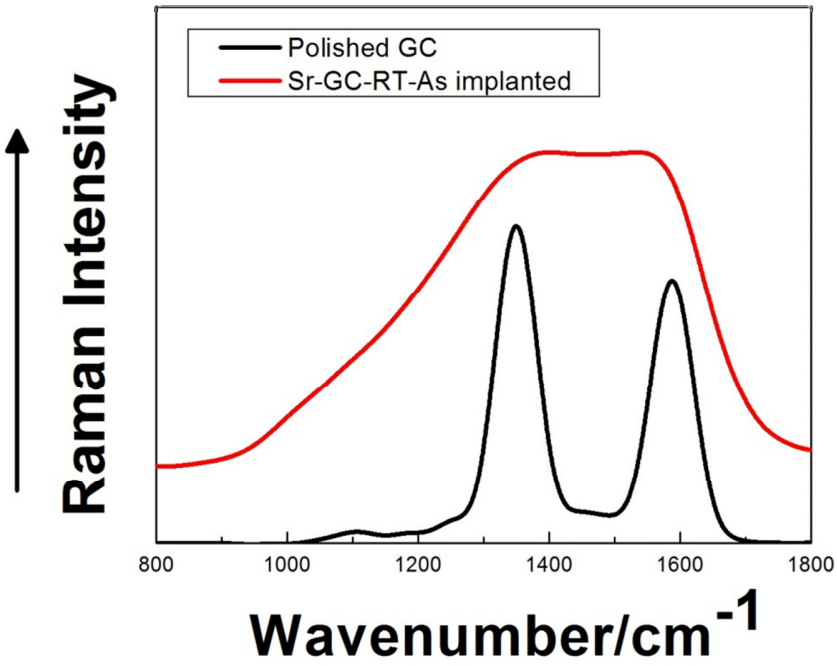

Figure 6.7: Comparative Raman spectra of polished (un-implanted) glassy carbon (black curve) and strontium implanted glassy carbon at room temperature (red curve).

Isochronal vacuum annealing (1 hour) of the strontium implanted samples in the same temperature range (i.e. 300 °C to 900 °C) as the above RBS investigation resulted in the broad "damage" peak encompassing the D and G peaks to remain - see Figures 6.8 and 6.9 . This indicates that most of the microstructural changes introduced in glassy carbon by the ion bombardment were not changed by the annealing. Superimposed on this broad peak, small peaks at approximately the D and G peak positions appeared after annealing at 300 °C – see Figure 6.8.

With increasing temperature the peaks became slightly more prominent and larger. At the lower annealing temperatures, i.e. up to 500 °C, the G (graphite) peak increased relatively more than the D (sp^3) peak indicating that any recrystallization or bonding that occurred due to the annealing were predominantly graphitic layer formation (sp^2 bonding). Annealing at 600 °C up to 900 °C and above resulted in a preferential growth, albeit still small, of the superimposed D peak. Niwase *et al*. [Niw92] studied the annealing of three HOPG samples bombarded with D^+ ions with different degrees of damage in the temperature range up to 600 °C. For the lightly damaged sample the D Raman peak decreased while the G peak increased with increasing annealing temperature. The highly damaged sample with the broad "damage" Raman peak behaved similarly to our Sr implanted glassy carbon. At about 300 °C a small G peak became visible and at the higher annealing temperatures the D peak also became superimposed on the broad band.

The above results, namely that there is only a slight annealing of radiation damage at these temperatures, are in agreement with those of Maruyama *et al*. [Mar92]. They irradiated glassy carbon and several carbons with neutrons and measured the thermal conductivity of the materials. Thermal conductivity is also often taken as a measure of radiation damage in graphite materials because the radiation defects act as obstacles for the phonon propagation thereby decreasing the thermal conductivity. Maruyama *et al*. found that the thermal conductivity of all their materials reduced to about the same value after relatively low fluence (i.e. above 0.25 dpa – displacements per atom) neutron irradiation indicating that all these carbon materials (including the glassy carbon) had similar irradiation-induced defects. Isochronal annealing resulted only in a very slight recovery in thermal conductivity up to annealing at about 1200 °C when a rapid increase was observed. However, even at 1700 °C the values were only about 78% of the unirradiated values. Essentially the same results were found by Snead *et al*. [Sne95]. and by Ishiyama *et al.* [Ish96]. Ishiyama *et al*. found that the thermal conductivity of neutron irradiated fine grained graphite progressively increases only at annealing temperatures above 800 °C. Burchell *et al*. [Bur11] measured the effect of annealing (500 °C, 1000 °C, 1500 °C and 2000 °C) on structural changes and electrical resistivity of neutron irradiated graphite. They observed only small annealing effects at annealing temperatures up to 1500 °C with more recovery at 2000 °C albeit still without full recovery. The above results are only valid for relatively high

fluences. Low fluence, i.e. below 0.1 dpa, irradiated carbon materials showed rapid recovery in thermal conductivities after low temperature annealing [Mar92], [Bar02], [Wu94].

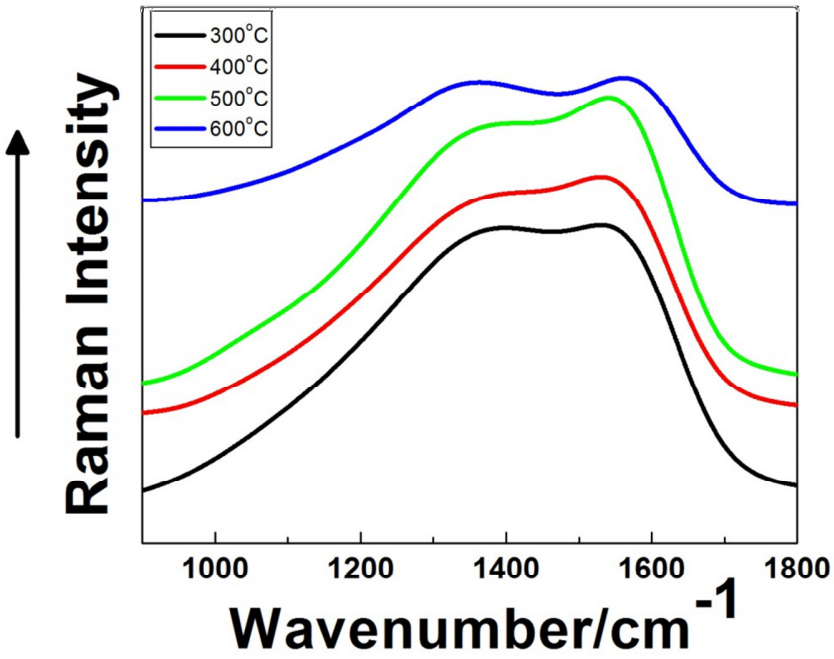

Figure 6.8: Raman spectrum of strontium implanted glassy carbon annealed from 300 °C to 600 °C for 1 hour.

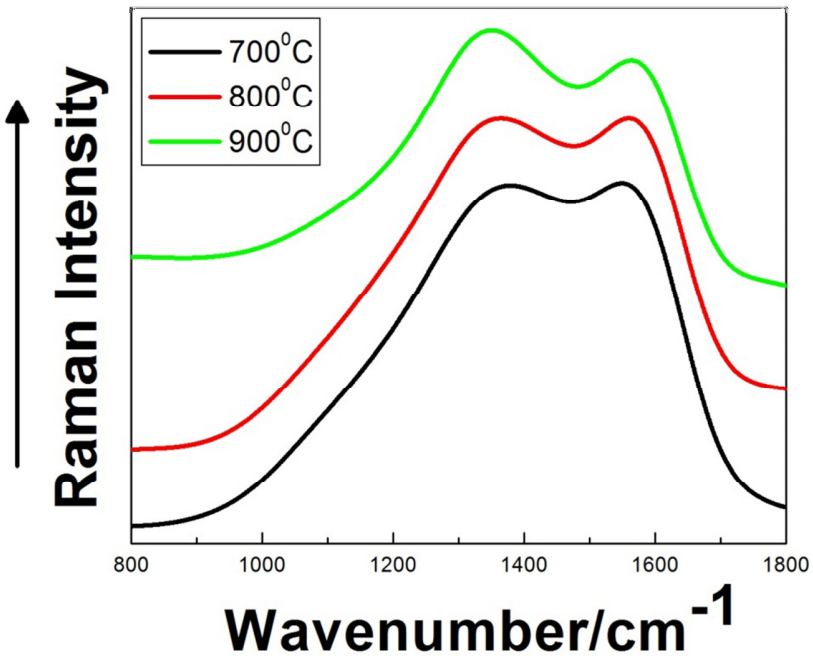

Figure 6.9: Raman spectrum of strontium implanted glassy carbon annealed from 700 °C to 900 °C for 1 hour.

A strontium implanted glassy carbon sample was annealed at 2000 °C for 5 hours and the corresponding Raman spectrum was compared with the polished GC spectrum – see Figure 6.10. The Raman spectrum shows that annealing the sample at 2000 °C for 5 hours resulted in partial recovery of the substrate. However, the sample does not return to the virgin spectrum. This is in agreement with results obtained by Burchell *et al*. [Bur11] as was discussed above.

It can be observed from Figure 6.10 that the intensity of the G peak became higher than that of the disorder peak after annealing at 2000 °C. This suggests that the sp^2 bonds became more predominant after heat treatment.

Table 6.2 gives the Raman spectra parameters obtained after fitting the Raman spectra shown in Figure 6.10 below using the Gaussian-Lorentzian fit. The ratio of I_D/I_G was 2.173 for the virgin glassy carbon sample and 0.741 for the annealed sample. The reduced I_D/I_G ratio for the annealed sample indicates an increase in sp^2/sp^3 ratio. This suggests that graphitization of the glassy carbon sample took place after heat treatment.

The FHWM values also show that the crystallite size increased after heat treatment at 2000 ^oC; usually, peaks with higher values of FWHM are considered to be more disordered.

Table 6.2: Raman spectra parameters for polished GC and Sr-GC-RT-2000 ^oC/5h.

SAMPLE	D PEAK Intensity	G PEAK Intensity	I_D/I_G	FWHM (D peak)	FHWM (G peak)
Polished GC	960.6	443.0	2.2	52.62	68.11
Sr-GC-RT-2000 ^oC-5h	731.0	975.2	0.75	44.51	39.52

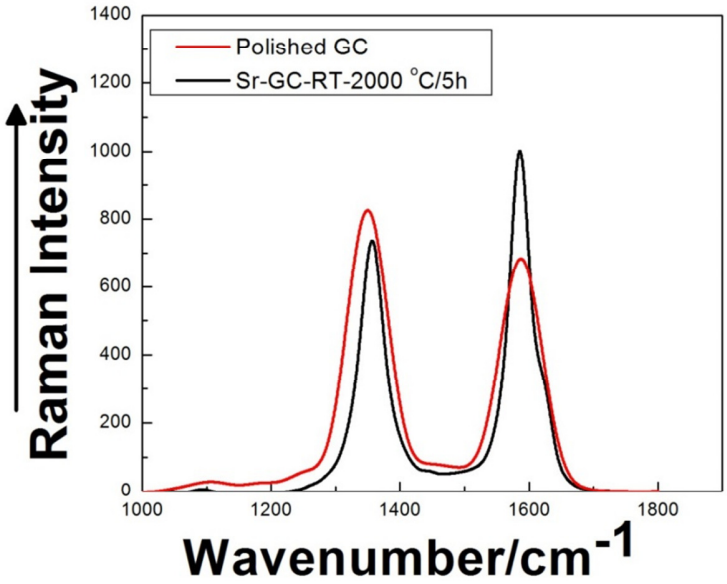

Figure 6.10: Raman spectrum of Polished GC and Sr-GC-2000 ^oC/5h

6.3 SCANNING ELECTRON MICROSCOPE (SEM) RESULTS.

Because surface topography can affect the RBS spectra, especially where broadening of the peaks is of interest, the topography of the sample was investigated using the scanning electron microscope.

Surface changes as a result of ion implantation and annealing were investigated and monitored using the scanning electron microscope in-lens micrographs. The effect of mechanical polishing on the surface of the glassy carbon was also studied

Figures 6.11(a) and (b) show the SEM micrographs obtained before and after polishing the glassy carbon sample. The unpolished glassy carbon sample is characterized by the presence of holes on the surface. In order to get rid of the holes, the sample was mechanically polished. The mechanical marks as a result of polishing can be seen in Figure 6.11 (b).

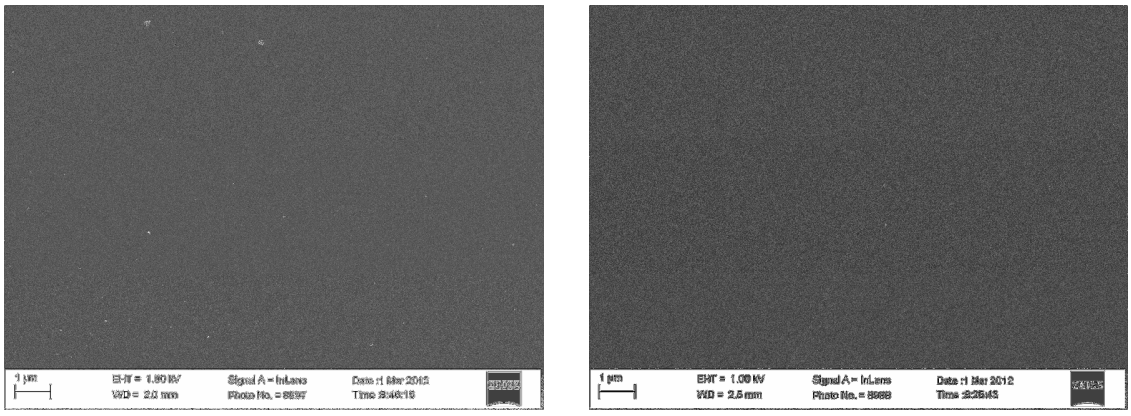

(a) **(b)**

Figure 6.11: SEM micrographs of (a) unpolished glassy carbon. (b) polished glassy carbon. Mechanical scratches can be seen in (b)

The effect of ion implantation is shown in Figure 6.12 below. The polishing marks became more prominent after heat treatment with some macro-pores being formed along the polishing marks;

This was because the some loose carbon atoms that were bounded to the surface of the sample during mechanical polishing were sputtered away during implantation.

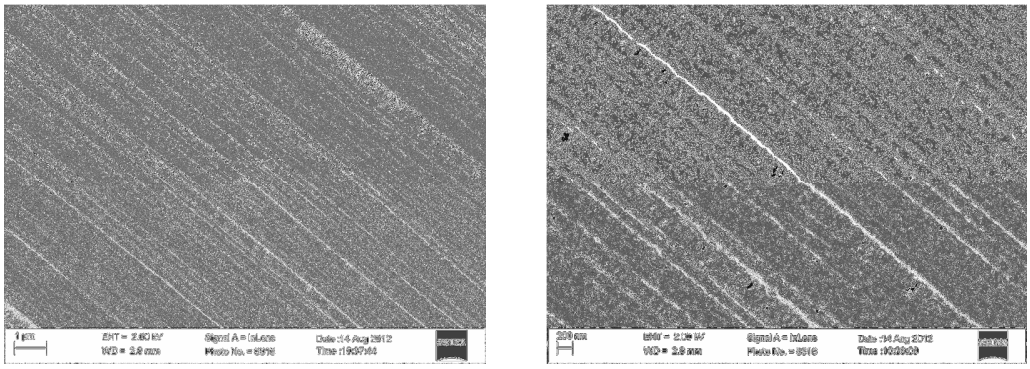

(a) **(b)**

Figure 6.12: SEM images for the As-implanted GC at: (a) lower magnification with size bar =1µm. (b) higher magnification with size bar = 200nm

The results acquired in this thesis are in agreement with the investigation carried out by Takahiro *et al*. [Tak03]. Takahiro et al. investigated the surface morphology of glassy carbon irradiated with nitrogen ions. The virgin glassy carbon and the implanted samples were viewed under the optical microscope. The polishing scratches and micro-pores became more prominent after irradiating the glassy carbon sample with nitrogen ions at 100 keV to a fluence of 4×10^{17} N^{+}/cm^{2}. The optical micrograph showed that the prominent polishing marks increased the surface roughness of the glassy carbon substrate.

Figure 6.13 shows the changes in the surface topography as a result of annealing. It was observed that the surface of the glassy carbon sample remained relatively unchanged after annealing i.e heat treatment had negligible effects on the surface and subsequently on the RBS results obtained.

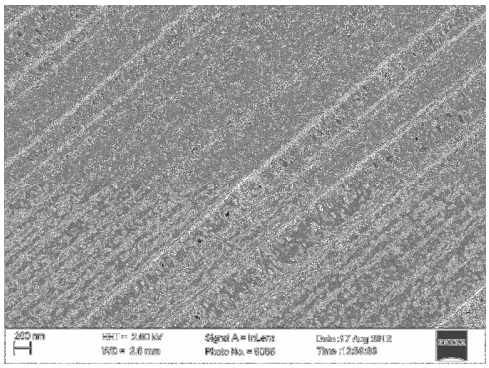

(a)

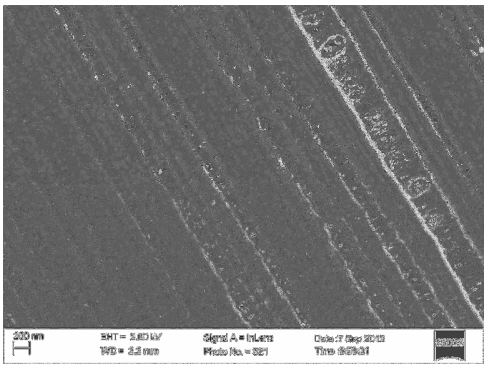

(b)

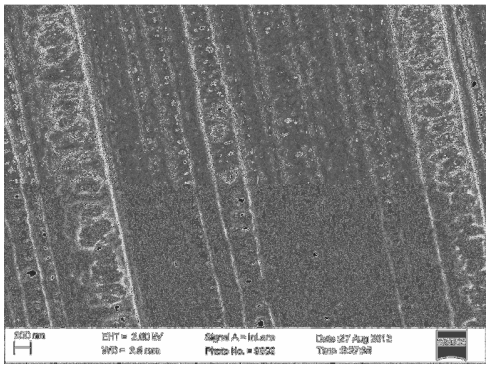

(c)

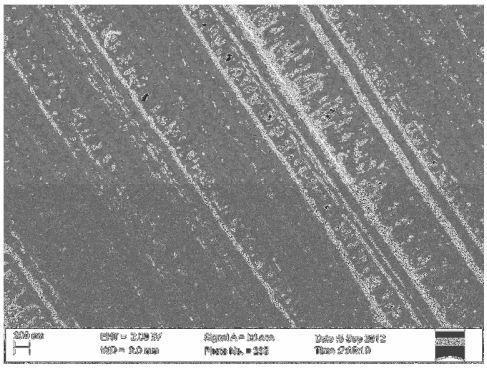

(d)

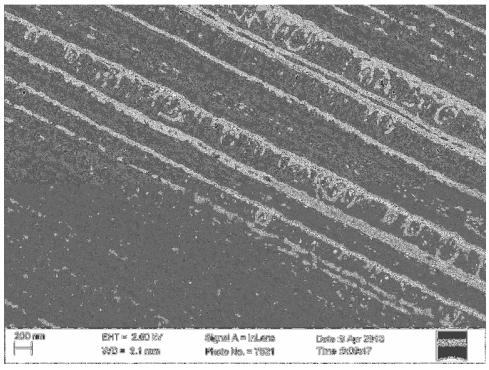

(e)

Figure 6.13: SEM micrographs of strontium implanted glassy carbon annealed at (a) 300 ^{o}C for 1 hour (b) 400 ^{o}C for 1 hour (c) 700 ^{o}C for 1hour (d) 800 ^{o}C for 1 hour.

6.4 REFRENCES

[Bar02] V. Barabash, I. Mazul, R. Latypov, A. Pokrovsky, C.H. Wu, Journal of Nuclear Materials 307 (2002) 1300.

[Bur11] T.D. Burchell, P.J. Pappano, J.P. Strizak, Carbon 49 (2011) 3.

[Fer00] A.C. Ferrari, J. Robertson, Physical Review B 61 (2000) 14095.

[Ish96] S. Ishiyama, T.D. Burchell, J.P. Strizak, M. Eto, Journal of Nuclear Materials 230 (1996) 1.

[Lan12] D.F. Langa, N.G. Van Der Berg, E. Friedland, J.B. Malherbe, A.J. Botha, P. Chakraborty, E. Wendler, W. Wesch, Nuclear Inst. and Methods in Physics Research, B 273 (2012) 68.

[Mar92] T. Maruyama, M. Harayama, Journal of Nuclear Materials 195 (1992) 44.

[McC94] D.G. McCulloch, S. Prawer, A. Hoffman, Physical Review (1994) 5905.

[Niw92] K. Niwase, T. Tanabe, I. Tanaka, Journal of Nuclear Materials 191 (1992) 335.

[Niw95] K. Niwase, Physical Review B 52 (1995) 15785.

[Sne95] L.L. Snead, T.D. Burchell, Journal of Nuclear Materials 224 (1995) 222.

[Tak03] K. Takahiro, R. Ookawa, K. Kawatsura, F. Nishiyama, S. Nagata, S. Yamamoto, K. Narumi, H. Naramoto, M. Iwaki, Nuclear Instruments and Methods in Physics Research Section B: Beam Interactions with Materials and Atoms 206 (2003) 206.

[Wu94] C.H. Wu, J.P. Bonal, B. Thiele, Journal of Nuclear Materials 212 (1994) 1168.

[Zie12] J.F. Ziegler, SRIM 2012 computer code, www.srim.org.

CHAPTER 7

CONCLUSION

Glassy carbon was implanted with strontium ions at room temperature to a fluence of 2×10^{16} ions/cm^2. Sequential isochronal annealing was carried out on the sample at 200 ^{o}C – 900 ^{o}C for one hour in vacuum. RBS was used to generate the depth profiles of the strontium implanted glassy carbon before and after heat treatment. The depth profiles were used to study the diffusion behaviour of strontium in glassy carbon. Raman spectroscopy was used to monitor the structural changes in the GC as a result of bombardment of strontium and heat treatment. SEM was also employed to monitor the corresponding surface modifications. All the results obtained from RBS, Raman spectroscopy and SEM led to the following conclusions.

The RBS depth profile of the implanted glassy carbon sample annealed at 200 ^{o}C for one hour was similar to that of the as-implanted profile. This was an indication that the annealing temperature was too low to cause any significant change in the strontium distribution. Fickian diffusion of strontium was observed when the annealing temperature was increased to 300 ^{o}C. The strontium depth profile remained Gaussian but no loss of strontium was recorded (within the experimental error) at this temperature. Annealing at 400 ^{o}C – 700 ^{o}C resulted in further diffusion of strontium towards the surface of the glassy carbon sample. This migration was accompanied with segregation of strontium on the surface of the GC. Loss of the segregated strontium was observed after the annealing temperatures were increased to temperatures greater than the melting point of strontium ~ 769 ^{o}C.

Raman spectrum obtained showed that implantation of strontium into GC damaged the GC substrate. The Raman D and G peak merged into a single broad band. Small peaks which are at approximately the D and G peaks position reappeared. The reappearance of these peaks implies that some of microstructural changes induced by strontium ion bombardment were annealed out. Annealing the sample at 2000 ^{o}C for 5 hours resulted in partial recovery of the substrate.

The SEM micrograph obtained after ion bombardment was compared to that of the polished GC and it was seen that the polishing marks became more prominent due to sputtering effect of the

bombarding ions. However, the surface of the GC remained unchanged after heat treatment. This shows that annealing had negligible effects on the surface of the GC and subsequently on the RBS results acquired.

7.2 PRESENTATIONS

This research has been presented in the following local and international conferences:

i. South African Institute of Physics (SAIP) conference that was held at the University of Pretoria, South Africa in 2012 (Poster presentation)
ii. South African Institute of Physics (SAIP) conference that was held at the University of Zulu land, South Africa in 2013 (Oral talk)
iii. International Conference on Ion Surface Interactions (ISI) that was held at the University of Yaroslavl, Russia in 2013 (Poster presentation)

7.3 FUTURE WORK

It has been stated earlier that segregation depends largely on Gibbs free energy; hence, Gibbs free energy calculations will be carried out theoretically in order to establish a theoretical base for understanding any segregation effects of the implanted species. Fickian diffusion of room temperature implanted strontium in glassy carbon at low annealing temperatures will also be investigated. This will be done by employing isothermal annealing technique.

Strontium ions will also be implanted in GC at elevated temperatures in order to investigate the effect of implantation temperature on diffusion and segregation.

Atomic force microscopy (AFM) will also be used to investigate the effect of ion implantation, heat treatment and segregation of implanted species on the surface roughness of the glassy carbon substrate.

Another aspect to be investigated will be the formation of nano-clusters of the implanted strontium in glassy carbon following post-implantation annealing and possible applications of such nano-clusters in glassy carbon. The interaction of slow highly charged ions with glassy carbon will also be investigated.